

Properties of Binary Systems in One-Dimensional Approximations and Applications

by

Ali Pourmand

A thesis submitted in partial fulfillment of the requirements for the degree of

Master of Science

Department of Physics
University of Alberta

© Ali Pourmand, 2023

Abstract

This thesis aims to provide a method to include the effect of the gravitational fields of binary systems when simulating them with one-dimensional stellar evolution codes. We also apply this method to simulate the evolution of binary systems until the donor fills its Roche Lobe.

The first part of this thesis is focused on describing the numerical code that was created to obtain several quantities related to binary systems. We then introduce a method that makes use of some of these obtained quantities to include the effects of a binary system's effective acceleration if one is evolving the stars a one-dimensional scheme. We provide a code that could apply this method in one-dimensional stellar evolution codes.

The latter part of the thesis is dedicated to utilizing this method to simulate binary systems up to the onset of the Roche lobe overflow. At this stage, this deviation should be most pronounced. We compare the evolutionary track produced by our method with what the standard treatment predicts. We find that the extent to which the donor stars differ at the Roche lobe overflow deviated between the techniques is sensitive to the stars' masses and the system's initial orbital separation. We also report an exceptional case where the final points could differ exceedingly. We finally simulate the possible progenitor of the V1309 Sco binary system and discuss the outcomes.

Preface

This thesis is an original work by Ali Pourmand in collaboration with professor Natalia Ivanova at the University of Alberta.

Chapter 2 contains text that has been accepted by ApJ for publication as “Properties of binary systems in a one-dimensional approximation”, Pourmand, A., and Ivanova, N. on May 7th, 2023. In this paper, I construct a method that allows one to simulate binary systems in a one-dimensional scheme. This work involved writing a numerical code that carries out simulations to create databases, including properties of binary systems. After verifying the accuracy of these obtained properties, another code, including the method to use these databases to simulate the effective acceleration of binary systems, was introduced, which is available for public use in https://github.com/AliPourmand/1D_binary_star_properties. The creation of the codes, plots, databases, and the derivation of the analytical terms resulted from my collaboration with N. Ivanova, who led the project.

Chapter 3 is devoted to using the code and databases created in Chapter 2 to simulate binary systems up to the Roche lobe overflow and discussing the outcomes. The simulations carried out and plots created in this chapter are my original work. Chapters 1 and 4, which are an introduction to the topic, and the findings of this thesis, respectively, are my original writing.

*To Eddington and Chandrasekhar, the two who wed stellar evolution to fundamental
physics and beautiful mathematics*

Acknowledgements

I would like to acknowledge Professor Natalia Ivanova for her support throughout my master's degree.

I would also like to acknowledge the emotional support my family members gave me, mainly my parents and sister Parisa, all of whom supported me remotely from the beginning of my studies.

Table of Contents

1	Introduction	1
1.1	Evolution of single stars	2
1.1.1	Timescales in Stellar Evolution	4
1.1.2	Energy Transfer Mechanisms	4
1.2	Stellar Evolution Codes	6
1.3	Binary Systems	6
1.4	Motivation	12
1.5	Observational Data	14
1.5.1	V1309 Scorpii	14
1.6	Thesis Objectives	15
1.7	Thesis Outline	15
2	Properties of Binary Systems in a One-Dimensional Approximation	17
2.1	Introduction	18
2.2	Binary in a corotating frame	20
2.2.1	Effective binary potential.	20
2.2.2	Effective acceleration.	22
2.3	One-dimensional representation	25
2.3.1	Volume-equivalent radii	26
2.3.2	Effective accelerations	28
2.3.3	Integration zones	29
2.3.4	Properties in the L_1 neighborhood cross-section	31
2.4	The numerical results	33
2.4.1	Self-convergence	33
2.4.2	Verification for Volume-Equivalent Radii	38
2.4.3	Verification for Effective Acceleration	38
2.4.4	Deviation of the binary effective acceleration from spherically symmetric gravitational acceleration	39

2.4.5	Deviation of the binary effective acceleration from the case of a solid body rotating star	39
2.4.6	Alternative treatment of the effective acceleration	41
2.4.7	How to use the provided quantities	42
2.5	Effects of a non-point mass	43
2.6	Conclusions	46
3	Application: Initial conditions of Common Envelope Events	56
3.1	Introduction	56
3.2	Modifying gravitational field in MESA	56
3.3	Grid of Simulations	57
3.4	Three Approaches	58
3.5	Results of the Grid Runs	59
3.5.1	Discussion	64
3.6	Initial Conditions Resulting in Extreme Deviations	64
3.7	Progenitor of the Observed Phenomena: V1309 Scorpii	67
4	Summary and Ongoing Work	70
	Bibliography	73
	Appendix A: Sample Inlists	76
	Appendix B: Sample Inlists for evolution up to RLOF	78

List of Tables

2.1	The properties computed and included in our database for each mass ratio.	49
2.2	The compact version of the database that will be used in B	50
2.3	The properties computed and included in our database for each of the first three Lagrange points.	50
3.1	Table including the mass ratios q (first row), final radii r_f (first column), and orbital separations (in solar radii) of our grid of initial conditions (the terms in parenthesis indicate the value of orbital separation for $M_1 = 3M_\odot$ stars which as explained, we have set their evolution to end at $45R_\odot$ instead of $50R_\odot$. Note that these selections will be used for each initial donor mass specified.	58

List of Figures

1.1	HR diagram for single stars. Solid lines show the evolutionary tracks of several single stars of different masses. The dashed line indicates the MS. Dot-dashed lines indicate the lines of constant radii, with their corresponding value denoted. The tracks have been obtained using MESA [9], [10], [11], [12],[13], [14], with a sample inlist used to obtain them provided in Appendix A	3
1.2	Color plots depicting the dimensionless potential ξ in a binary corotating frame for two mass ratios: $q = 0.5$ and $q = 4$, from top to bottom. Plots show 2D slices in the xy -plane (left panels) and xz -plane (right panels). The color bar represents the chosen range of values of the scaled potential ξ at each point. The white areas are where ξ is outside the scope of interest for our work. The coordinates are in units of the orbital separation, and the Lagrange points have been denoted by Li	9
1.3	Plots of the contours of the dimensionless effective acceleration η , in a binary corotating frame, for two mass ratios: $q = 0.5$ and 4, from top to bottom. Shown are slices in the xy -plane (left panels) and xz -plane(right panels). The coordinates are in units of the binary separation, and the Lagrange points have been labeled by Li . As can be seen, near the center of the two stars, the gradient of change in the values of η is much steeper, and the shape of the contours is much more spherically symmetric.	10
1.4	Shown are the evolutionary tracks of the donor star, $M_1 = 3M_\odot$, evolved in a binary system with the companion star if $M_1 = 3M_\odot$. The initial orbital separations in the case shown with the red solid line is $a = 11.36R_\odot$, and the donor started the MT. In the case shown with the black dashed line, the initial orbital separation is too large to initiate the MT during the shown evolution. The tracks were obtained using the binary module available in MESA [11].	11

1.5	Schematic depicting two of the possible outcomes of the CE phase. The upper right shape shows when envelope ejection is successful, and a compact binary is formed. The lower right depicts a merger scenario.	13
2.1	Two-dimensional slices showing the scaled potential ξ in a binary corotating frame for three mass ratios: $q = 0.2, 2$, and 5 , from top to bottom. Shown are slices in the xy -plane (left panels) and xz -plane (right panels). The color bar represents the chosen range of the scaled potential ξ at each point. We plot a narrow range of equipotentials for a better resolution in the region of interest; the white areas are where ξ is outside the chosen ranges. The coordinates are in units of the orbital separation, and the Lagrange points have been denoted by Li . The black line passing through L_1 is the L_1 -plane (the plane through the first Lagrange point and perpendicular to the line attaching the two stars). The equipotential surfaces passing through L_1, L_2 , and L_3 are shown with black lines.	21
2.2	η_x, η_y , and η_z shown for mass ratio $q = 2$. The coordinates are in units of the orbital separation.	23
2.3	Two-dimensional slices showing the contours of the effective acceleration η , in a binary corotating frame, for three mass ratios: $q = 0.2, 2$, and 5 , from top to bottom. Shown are slices in the xy -plane (left panels) and xz -plane(right panels). The coordinates are in units of the binary separation, and the Lagrange points have been denoted by Li .	24
2.4	A sample equipotential surface outside of the Roche lobe in a binary star with the mass ratio $q = 2$, shown in blue color. The equipotential surface is limited by the L_1 -plane, shown in red color. The coordinates are in units of the orbital separation.	26
2.5	A depiction of a part of the equipotential shell with triangular meshes on it shown in 3D; for a random shell in the case of the mass ratio $q = 0.5$. Only a part of the integration domain is shown, to make the triangular mesh visible.	28
2.6	The three zones of integration; this specific example is for a mass ratio of $q = 2$. The zones are defined as described in equation 2.19, see § 3.3 for further details.	29
2.7	The intersection of several equipotential surfaces with the L_1 plane for $q = 0.2$. Axes are in units of the orbital separation.	32

2.8 This plot shows the results of our highest resolution run for the volume equivalent radii passing the first three Lagrange points, as a function of the mass ratio. The horizontal axis is in the units of orbital separation. R_{L3} volume around the donor star exists only for mass ratios greater than 1. Note that the outer Lagrange point is L_3 for mass ratios greater than 1, and is L_2 for mass ratios less than 1. 33

2.9 Self-convergence test for the effective acceleration for mass ratios $q = 2$. The vertical axis is the normalized error in effective acceleration for angular resolutions $m = 500, 1000, 2000$, and 4000 (Equation 2.20). The horizontal axis is F , the fill-out factor F (Equation 2.21). $F > 1$ means the equipotentials are outside of the Roche lobe. 34

2.10 Self-convergence test for the volume-equivalent radius for mass ratio $q = 0.2$. The vertical axis is the normalized error in volume equivalent radius at L_1 for angular resolutions $m = 500, 1000, 2000$, and 4000 (Equation 2.20). The horizontal axis is the fill-out factor F (Equation 2.21). 35

2.11 Deviation of R_{L_1} (L_1 volume-equivalent radius) from [19] relation (the blue line). Deviation of R_{outer} (the outer Lagrange equipotential volume-equivalent radius) from the one provided by the Equation 2.22 (the orange line). The deviations are shown as functions of mass ratio q 37

2.12 The deviation in effective acceleration from our tables for mass ratios $q = 0.2$ (the left plane) and $q = 2$ (the right plane), as a function of the volume equivalent radius. The red star denotes the equipotential passing L_1 . The green curve in each figure is the analytical expression 2.40. We show the analytical solution for the distances within 0.5 of R_{L1} , albeit we use it only for the distances within 0.05 of x_{L_1} , as described in the text. One can see that the analytical solution matches the numerical solution for a large range of distances. The blue line shows the case when the effective acceleration is average over the whole contour surrounding the star, and the orange line shows the effective acceleration with L_1 plane is excluded from the averaging. 39

2.13 The deviation in effective acceleration from our tables from a solid body rotating star, as a function of the mass ratios (blue circles). The deviation is provided for stars that fill their Roche lobe. With orange stars, we show the deviation where we used Eggleton’s equation for Roche lobe radius instead of our integrated quantities for the spherically symmetric acceleration and the rotating term. See §2.4.5. 40

2.14	The effective gravity averaged over equipotential multiplied by the inverse effective gravity averaged over equipotential, as a function of the mass ratios. See §2.4.6.	41
2.15	The simplified effective acceleration and the integrated effective acceleration, as a function of R_{eq} , for polytropes with $n = 3$ (blue line) and $n = 1.5$ (orange line). Shown for the case $q = 1$	45
3.1	Position on the HR diagram of the simulations with $q = 0.5$ when the donor star has reached Roche Lobe Size. The red star indicates the final point using method 1, the blue diamond indicates method 2, and the purple triangle indicates the result using method 3 (the three methods were explained in 3.4). The solid black lines depict the evolutionary tracks of single stars with the same initial conditions the donor star has. The black dashed line is the MS branch.	60
3.2	Figure similar to figure 3.2, for mass ratios $q = 1$	61
3.3	Figure similar to figure 3.2, for mass ratios $q = 2$	62
3.4	Figure similar to figure 3.2, for mass ratios $q = 10$	63
3.5	HR diagram showing evolutionary tracks for the donor star in the binary system described in Section 3.6 ($M_1 = 3M_{\odot}$, $q = 10$, and $a = 22.14R_{\odot}$), evolved up to the Roche Lobe size. The evolutionary tracks were obtained with the three methods described in Section 3.4.	65
3.6	The adiabatic and radiative exponents that the 3 methods predict once the donor star described in Section 3.6 reaches the Roche Lobe size. Adiabatic exponents ∇_a are shown by the blue line, and Radiative exponents ∇_r are depicted with the orange line.	66

3.7	Kippenhahn diagram showing the evolution of internal structure of the donor star in the binary system described in Section 3.6 ($M_1 = 3M_\odot$, $q = 10$, and $a = 22.14R_\odot$). The horizontal axis shows the evolutionary time passed throughout the simulation in Mega years, and the vertical axis indicates the mass coordinate of the star. In a Kippenhahn diagram, different colors are used to differentiate between the physical processes happening in each mass coordinate. The abbreviations of these physical processes are written in color used to visualize them under the horizontal axis. The most notable physical processes in this star's evolution are convective areas (light blue), nuclear burning (light red), and overshoot (cream). Towards the very end of the evolution, an external convective area has formed. This plot was created with MESA's package for visualization <code>pgstar</code> [36].	67
3.8	Evolutionary tracks of V1309 Sco.	68

Chapter 1

Introduction

Binary stars are stellar systems consisting of two stars that are gravitationally bound together, and thus orbit around each other. Binary systems aren't rare to be found. For example, recent findings have shown that about 70% of massive stars will not only have a companion star but also their evolution will be affected by the companion's presence [1]. Even for solar-like stars, studies have shown that in catalogs such as Hipparcos, about $56\% \pm 2\%$ of the data are single stars, with the rest having one or more companions [2]. Studying binary stars comprises a distinct and active area in astronomy.

What has made studying these systems more interesting during the past years is that binary stars provide a major channel for the formation of exotic astronomical phenomena. Such phenomena include merger events of neutron stars due to their orbital decay due to gravitational wave radiation [3]. In the dawn of gravitational wave detectors such as The Laser Interferometer Gravitational-Wave (LIGO) and The Laser Interferometer Space Antenna (LISA), theoretical astrophysics is aiding the observations by answering fundamental questions such as the following one: what is the frequency of gravitational waves events we expect to detect from different astrophysical sources? Two examples in literature that have carried out such studies are [4], who estimated the rates of compact object merger events possibly observable by LIGO, and [5], who discussed the prospects of detecting gravitational waves from

the Common Envelope (CE) phase.

Answering this question relies on the ability to accurately predict the fate of the evolution of stars in binary systems, and has been carried out by studies such as [6] in the past. However, the uncertainties of the outcome of certain evolutionary phases in binary stellar evolution, most notably the common envelope (CE) phase, have impeded studies such as the one mentioned for accounting for the contribution of this phase with proper theoretical backing. The natural prerequisite for understanding binary stellar evolution is the knowledge of how single stars evolve. In the following, we will briefly describe key concepts in stellar structure and evolution of single stars before moving on to the several specific issues that the binary stellar evolution introduces.

1.1 Evolution of single stars

The evolution of single stars is a well-developed field. What is helpful is that the life of a single star mainly depends on only two parameters, the initial mass and chemical composition (rotation could influence the evolution to some minor extent as well [7]). One of the best tools used to depict stars' evolution is to plot their effective temperature T_{eff} , and surface luminosity, L , at each step of their evolution. Such a plot is known as the Hertzsprung-Russell (HR) diagram. The HR diagram depicting the evolution of several stars with different initial masses is provided in Figure 1.1. The dashed line is known as the Main-Sequence (MS). On the MS, stars live while using Hydrogen nuclear burning as the energy source. The MS phase of stellar evolution is the most long-lasting phase of stellar evolution [8]. Stars of different masses begin their MS lives on the HR diagram at the different locations at the MS. The tracks on the HR diagram that originate at the MS correspond to the evolution of the stars after the MS. Please note that the lengths of segments of these lines do not indicate the time spent during corresponding evolutionary stages.

Stars remain in hydrostatic equilibrium (HE) for most of their evolutionary time,

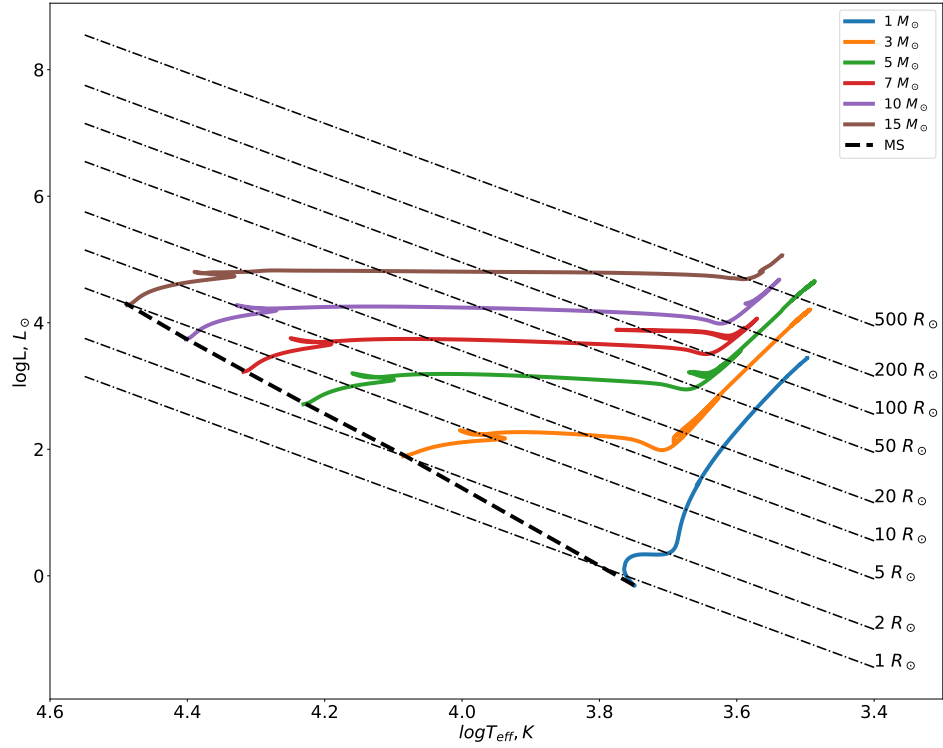


Figure 1.1: HR diagram for single stars. Solid lines show the evolutionary tracks of several single stars of different masses. The dashed line indicates the MS. Dot-dashed lines indicate the lines of constant radii, with their corresponding value denoted. The tracks have been obtained using MESA [9], [10], [11], [12],[13], [14], with a sample inlist used to obtain them provided in Appendix A

meaning that usually gravity and pressure balance each other. The concept of HE is quantified inside single stars with the following equation:

$$\frac{dP}{dr} = -\frac{Gm\rho}{r^2}, \quad (1.1)$$

where P is pressure, r is the radius of the zone, m is the mass of the star up to the radius r , ρ is the density of that zone, and G is the gravitational constant.

The following sections will explain two important concepts that will be useful in our future studies.

1.1.1 Timescales in Stellar Evolution

A helpful set of terminology is commonly used among astrophysicists to evaluate the time it takes for notable changes to happen during the evolutionary stages. The three main timescales are the following:

1. The Nuclear Timescale, τ_{nuc} .
2. Thermal Timescale, also known as Kelvin-Helmholtz (KH) Timescale, τ_{KH} .
3. Dynamical Timescale, τ_{dyn} .

For stars, almost always the following inequalities are valid (apart for exceptional stages such as supernovae explosions)

$$\tau_{\text{nuc}} \gg \tau_{\text{KH}} \gg \tau_{\text{dyn}}. \quad (1.2)$$

1.1.2 Energy Transfer Mechanisms

The energy created in the star's core eventually gets transferred to the star's surface, resulting in its apparent luminosity. The transfer of energy takes place using 3 main processes, which are:

1. Convection

2. Radiation

3. Conduction (only important in regions of stars with degenerate matter [8]. Since in normal stellar material it doesn't play a major role, it will hereafter be neglected in our study.)

The mechanism that dominates the energy transfer inside a star may vary from region to region. Moreover, the location, both in mass and in radius, for each energy transfer mechanism changes throughout the star's evolution. For example, a star with $5M_{\odot}$ initially has a convective core and radiative envelope on its MS. When the star enters the giant phase, it has a radiative core and convective envelope.

The energy transfer mechanisms are often used to interpret which is the core and what is the envelope. The standard tool to differentiate between adiabatic convective regions and radiative regions is the Schwarzschild criterion. According to the Schwarzschild criterion, the condition necessary for a region to undergo radiative energy transportation rather than convective energy transport is:

$$\nabla_r < \nabla_a . \tag{1.3}$$

Here ∇_a is the temperature variation a gas element undergoes during an adiabatic change in pressure, also known as the adiabatic exponent:

$$\nabla_a = \left. \frac{d \log T}{d \log P} \right|_{\text{ad}} \tag{1.4}$$

∇_r is the radiative temperature gradient. It shows how the temperature change with a pressure change if all the energy transportation is radiative. It is defined as

$$\nabla_r = \left. \frac{d \log T}{d \log P} \right|_{\text{rad}} \tag{1.5}$$

1.2 Stellar Evolution Codes

Non-rotating stars are spherically symmetric. Stellar properties such as pressure, temperature, density, etc., are only functions of the distance to the center. One could use a simplified set of stellar structure equations to model the evolution of stars for the periods where HE is in place. There has existed for a long time a plethora of stellar evolution codes to simulate the evolutionary tracks of stars [15], [16], [17]. The stellar evolution codes that work under the assumptions of spherical symmetry are usually referred to as one-dimensional (1D) stellar evolution codes.

One of the most popular 1D stellar evolution codes that are used nowadays is the Module for Experiments in Stellar Astrophysics, **MESA**, package [9], [10], [11], [12],[13], [14]. **MESA** has several qualities that have increased popularity in the community during the past few years: it is free and open-source and includes a vast library of physics one could choose to use. Most importantly, one can include additional equations, modifying the adopted physics model. Due to the latter, **MESA** is the code we will use throughout this work.

1.3 Binary Systems

The fate of stars in binary systems couldn't be classified as straightforwardly as could be done for single stars. That is due to several complexities which require some explanation. Along with the mass, rotation, chemical composition, and age of the two stars, the influencing parameters affecting the evolution of stars in a binary system are orbital separation and eccentricity. The mass ratio q of the two stars in the system is another important quantity in determining the evolutionary outcome. The mass ratio is defined as

$$q = \frac{M_1}{M_2}, \quad (1.6)$$

where M_1 and M_2 are the two stars' masses. In the following, we will refer to M_1 as the donor star, and M_2 as the companion star.

The first aspect that makes binary stars' evolution different from single stars is that they no longer experience only the spherically symmetric gravitational force. The companion star's gravitational pull, along with the centrifugal forces due to the orbital motion of the stars around their center of mass, is also felt by both the donor star and the companion star. The effective potential Ψ of a point with coordinates (X, Y, Z) in the vicinity of a binary system. It is given with the following equation (in the corotating frame, and assuming the orbital plane is the xy -plane):

$$\Psi(X, Y, Z) = -\frac{GM_1}{|R_1|} - \frac{GM_2}{|R_2|} - \frac{1}{2}\Omega^2 \left[\left(X - a\frac{M_2}{M_1 + M_2} \right)^2 + Y^2 \right]. \quad (1.7)$$

Here M_1 and M_2 are the donor and companion star masses, a is the orbital separation, $\Omega = \sqrt{G(M_1 + M_2)/a^3}$ is the binary system's orbital angular velocity, and R_1 and R_2 are the distances of each element to the donor star's and companion star's centers:

$$\begin{aligned} |R_1| &= \sqrt{X^2 + Y^2 + Z^2}, \\ |R_2| &= \sqrt{(X - a)^2 + Y^2 + Z^2}. \end{aligned} \quad (1.8)$$

The effective acceleration (we will be using this term instead of gravitational acceleration for binary stars since it doesn't only constitute the effects of gravity anymore) g_{eff} could be obtained in the following way:

$$g_{\text{eff}} = -\nabla\Psi. \quad (1.9)$$

One useful way to rewrite these two variables is if we make them dimensionless. To do so, we use the scaling factor used in [18] to define a dimensionless potential ξ , and dimensionless effective acceleration η :

$$\begin{aligned}\Psi &= -\frac{G(M_1 + M_2)}{2a}\xi \\ g_{\text{eff}} &= -\frac{G(M_1 + M_2)}{2a^2}\eta.\end{aligned}\tag{1.10}$$

Figures 1.2 and 1.3 depict contours for ξ and η in the xy -plane and xz -plane, respectively, for stars with several different mass ratios. As can be seen in the figures, the closer to the donor star’s center, the closer the effective potential and acceleration to spherical symmetry. The further from the center, the more contours deviate from the spherical shape and turn into a teardrop shape once they reach the first Lagrange Point $L1$. Lagrange Points are points in which the effective acceleration felt is zero. They are denoted by Li , with i being the index starting from the highest potential. From the shown shape of effective acceleration, it is reasonable to assume that stars whose size are much smaller than the size of the Roche Lobe (the equipotential surface passing $L1$), don’t feel an effective acceleration much different from a single star. However, this deviation may become notable for stars close to filling their Roche Lobes (the situation we are mainly interested in; see 1.4). Roche Lobe Overflow (RLOF) is the term used to describe the phenomena when a star in a binary system has filled its Roche Lobe. Eggleton found a numerical fit relating the size of the Roche Lobe to the mass ratio and orbital separation by computing the volume of the Roche Lobe V_{RL} for different mass ratios and equated this volume with the volume of the sphere to obtain the “volume-equivalent radius” of the Roche Lobe, also known as the Eggleton radius [19], which we will denote with R_{L1} .

The second issue that makes the evolution of binary stars different from single stars is the possibility of mass transfer (MT) phenomena between the two stars. It is well known that stars expand notably in some stages of their evolution. Suppose the star expanded enough to exceed its Roche Lobe in size¹. In that case, the outer layers

¹this threshold is checked in 1D stellar codes by comparing the radius of the star and the Eggleton radius

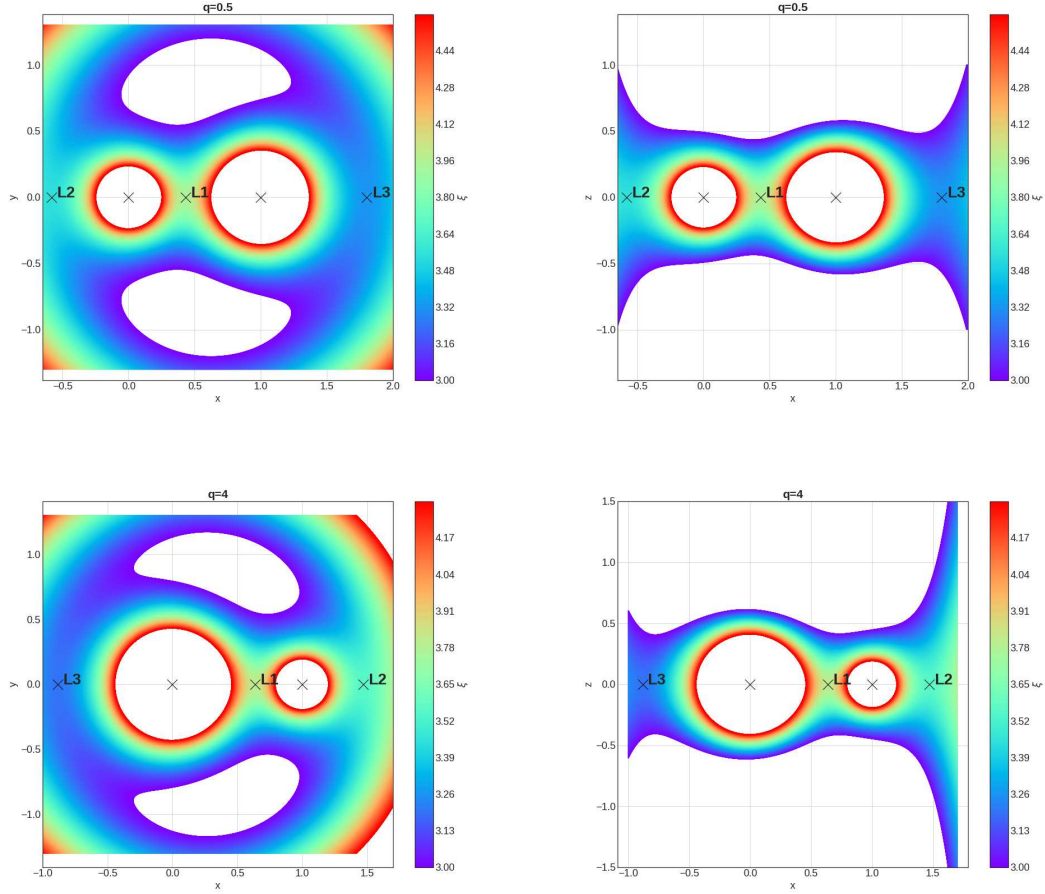


Figure 1.2: Color plots depicting the dimensionless potential ξ in a binary corotating frame for two mass ratios: $q = 0.5$ and $q = 4$, from top to bottom. Plots show 2D slices in the xy -plane (left panels) and xz -plane (right panels). The color bar represents the chosen range of values of the scaled potential ξ at each point. The white areas are where ξ is outside the scope of interest for our work. The coordinates are in units of the orbital separation, and the Lagrange points have been denoted by L_i .

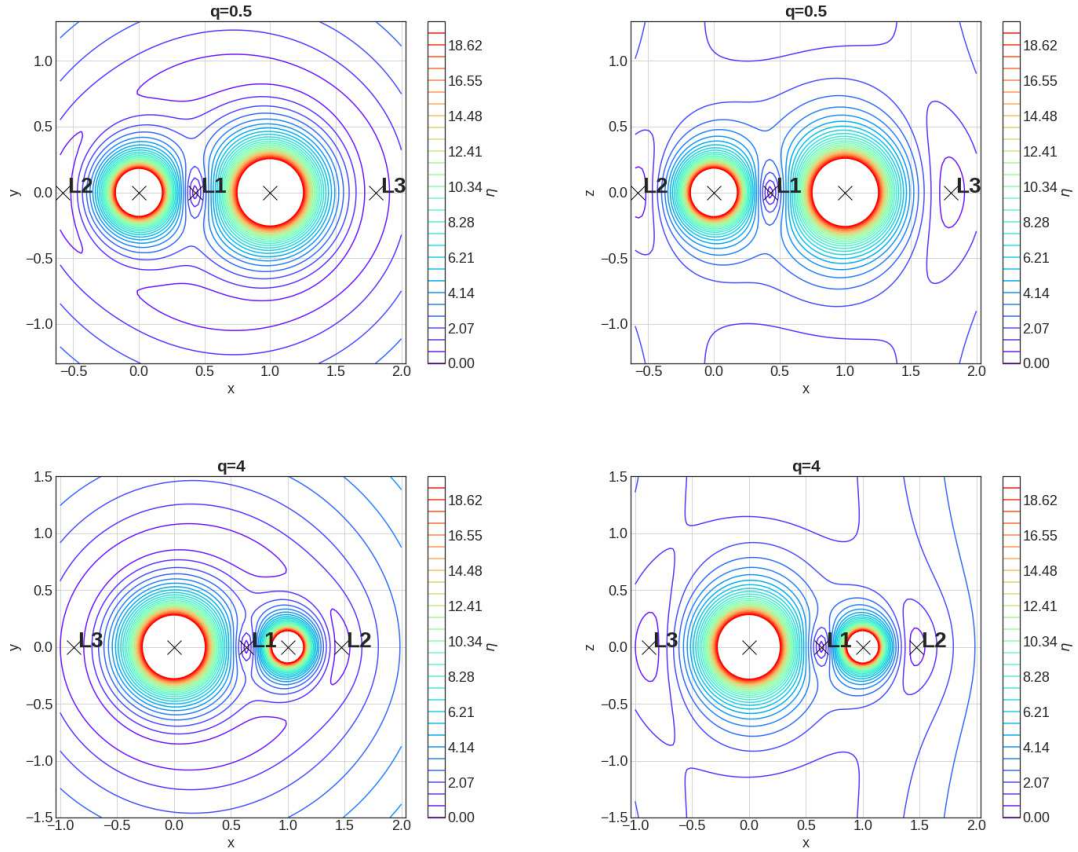


Figure 1.3: Plots of the contours of the dimensionless effective acceleration η , in a binary corotating frame, for two mass ratios: $q = 0.5$ and 4 , from top to bottom. Shown are slices in the xy -plane (left panels) and xz -plane (right panels). The coordinates are in units of the binary separation, and the Lagrange points have been labeled by L_i . As can be seen, near the center of the two stars, the gradient of change in the values of η is much steeper, and the shape of the contours is much more spherically symmetric.

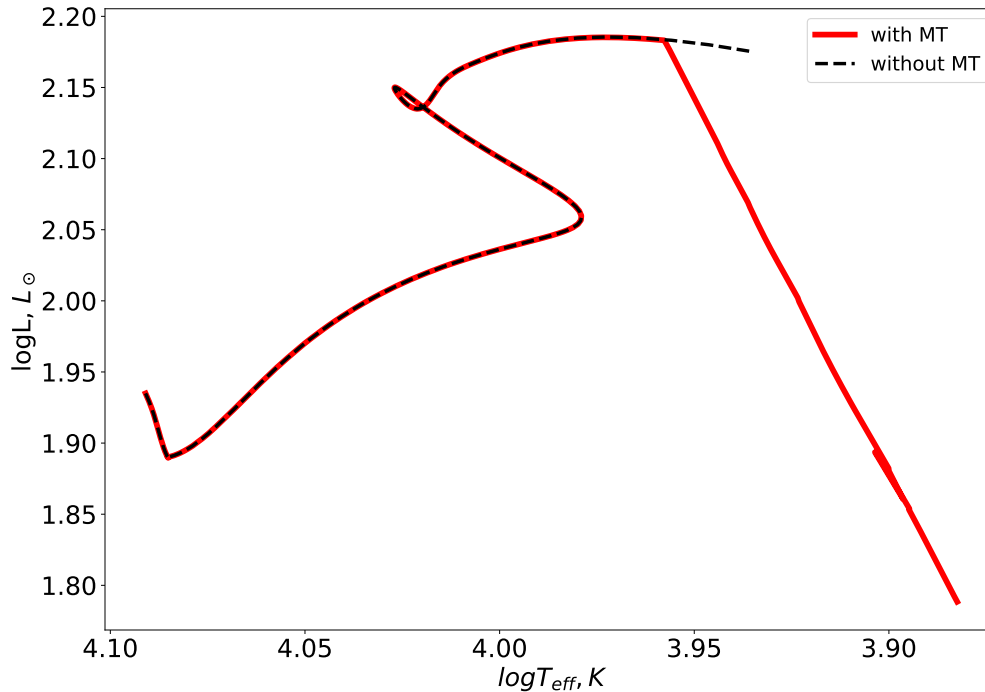


Figure 1.4: Shown are the evolutionary tracks of the donor star, $M_1 = 3M_\odot$, evolved in a binary system with the companion star if $M_1 = 3M_\odot$. The initial orbital separations in the case shown with the red solid line is $a = 11.36R_\odot$, and the donor started the MT. In the case shown with the black dashed line, the initial orbital separation is too large to initiate the MT during the shown evolution. The tracks were obtained using the binary module available in MESA [11].

of the donor star that are close to the companion star are no longer bounded by the gravitational pull of the donor star and will start to be attracted by the companion star. Relocation of the donor’s mass to the companion, or the mass transfer (MT), will change the mass ratio of the system. In some cases, MT could drastically change the evolutionary tracks of binary stars from single stars (as an example, see figure 1.4).

There are other effects that play a role in binary stellar evolution that are absent in the evolution of single stars: magnetic braking, gravitational waves, and, most important for this thesis, tidal evolution. As mentioned previously, although the main factor determining the evolution of stars is their initial mass, the rotational velocity of

stars could also affect the evolutionary tracks to some extent [20]. In binary systems, the angular frequency of the two stars is influenced by tidal interactions between the two stars. The physical principle behind tidal effects is that stars are not point objects, which results in a torque being exerted upon each star. The exertion of this torque results in the evolution of the angular rotation (for more information on the equations that govern tidal evolution, see [21], and [22]).

Tidal effects and other processes specific to binary systems have been incorporated in MESA [11]. However, MESA’s binary package does have some shortcomings. For example, the effective acceleration used for stars in a binary system is the same as if each star was single.

1.4 Motivation

As described previously, once a star in a binary system overfills its Roche Lobe, the MT will initiate. The MT could be stable or unstable, depending on the circumstances. If the mass transfer is unstable and occurs on the order of τ_{dyn} , the binary system may enter an evolutionary phase known as the CE phase [23]. The phase got this name because the companion star finds itself orbiting inside the expanding envelope of the donor star – they share a “CE”. Once the companion star starts to orbit inside the envelope, the orbital energy is transferred from the orbit to the envelope. This results in even faster orbital decay. The CE phase could result in either the merger of the two stars or the ejection of the envelope accompanied by the formation of a compact binary. For a more comprehensive picture of the possible endings of binary stellar evolution, refer to [24]. Figure 1.5 shows a schematic illustration of the two mentioned outcomes.

We are interested in constructing a precise picture of binary stars at the initial stage of their CE phase to cast more light upon the fate of binary stars. To do so, we can choose one of the tools used in theoretical astrophysics, 1D stellar evolution codes, or 3D hydrodynamical codes.

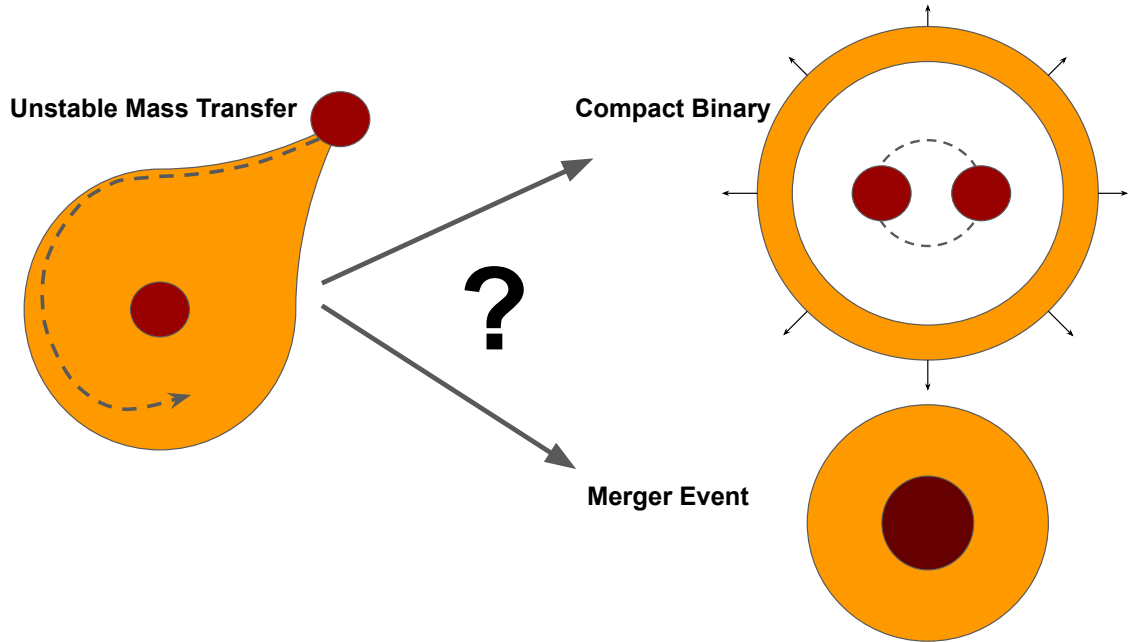


Figure 1.5: Schematic depicting two of the possible outcomes of the CE phase. The upper right shape shows when envelope ejection is successful, and a compact binary is formed. The lower right depicts a merger scenario.

The time it takes for binary stars to reach the beginning of the CE phase is often similar to its nuclear timescales τ_{nuc} . Since we know that $\tau_{\text{nuc}} \gg \tau_{\text{dyn}}$, 3D hydrodynamical codes are impractical to use for this purpose, as they are only efficient for events that take place on the order of dynamical timescales. Furthermore, they don't handle aspects of stellar physics such as convective and radiative energy transport, or nuclear reactions.

In binary systems, HE is preserved at least until CE initiates. That allows us to use 1D stellar evolution codes for the evolution prior to the CE. However, the gravitational effect of the companion star and the centrifugal forces also have to come into the picture. Moreover, when one of the stars gets comparable in size to the Roche Lobe, it gets notably deformed from spherical symmetry. Hence, 1D stellar evolution codes have to be modified.

1.5 Observational Data

Relating CE theory to observations isn't straightforward, mainly due to its duration's short timescale ($\sim \tau_{\text{dyn}}$). It doesn't mean, of course, that we can not relate CE with observations. Historically speaking, Paczynski used a CE phase as the mechanism to explain the existence of compact (short-period) binaries [25]. Compact binaries are two evolved stars orbiting each other at a short distance. This orbital separation is smaller than the radius these evolved stars would have had if their evolution followed what single stellar evolution predicts. The puzzle as to how such observed systems could be formed was solved with the proposal of the CE theory. Therefore, from its inception, this theory was not based on direct observations of a CE phase but on the observations of its consequences.

In the following section, we will describe a binary system known to have gone through a merger event. This system makes a good specimen to investigate how good of an assumption it is to ignore the effects of the binary gravitational field.

1.5.1 V1309 Scorpii

V1309 Scorpii is an exceptional case in the history of binary stellar evolution. It is the first direct observation of a binary system that ended in merging the two stars into a single object [26]. A relatively sudden outburst was recorded from a region of the sky at the time of this merger event. Before this, several years of observational data were available for the region of the sky in which this outburst was observed. Based on those observations, it was indicated that prior to this outburst, a binary system with an orbital period of about 1.4 days existed there [26]. It was also established that the system's orbital period had been decaying over time prior to the outburst. These findings support the theory that this outburst resulted from a merger event of two stars in a binary system.

Based on the works of [27], who calculated a grid of initial conditions to find a match

to the observed properties of the progenitors, it could be assumed that the progenitor binary had a mass ratio of $q \approx 10$ and a donor star mass of about $M = 1.52M_{\odot}$.

Studies such as [28] have attempted to simulate the outcome of the merger event of this system. However, these studies focus on simulating the events following the onset of the CE phase. Before our study, such studies usually used stars evolved using a single gravitational field up to the Roche Lobe size. It is unclear how good of an assumption this is.

1.6 Thesis Objectives

Our study’s primary goal is to obtain properties of binary systems at the onset of the CE phase. To do so, we must develop a physically valid method to evolve binary systems. The main issue with creating such a method is that the effective acceleration that binary stars feel deviates from a single star’s gravitational field, especially the stars that are close to filling their Roche Lobe. Therefore, we cannot use MESA’s standard binary package, as it neglects the effect of centrifugal forces and the companion star in the binary system’s effective acceleration.

Our study consists of two parts. First, we develop the method that takes into account the effects of the companion star and the centrifugal forces while evolving stars in binary systems. Second, we use our novel method to model stellar evolution up to the start of the MT, to see how much this previously neglected physics could change the expected outcomes.

1.7 Thesis Outline

Our thesis is organized in the following way: in § 2 we describe how to obtain properly 3D reduced binary effective acceleration for 1D stellar codes.

§ 3 is devoted to applying our method developed in § 2. We discuss how stellar evolution changes using our 3D-reduced binary approximation if compared with the

existing approaches. The discussion uses a grid of stellar models and then goes into detail for the two specific observed systems.

In § 4 is the conclusion and the discussion of the possible future work.

Chapter 2

Properties of Binary Systems in a One-Dimensional Approximation

ALI POURMAND¹ AND NATALIA IVANOVA¹

¹*Department of Physics, University of Alberta, Edmonton, T6G 2E7, Alberta,
Canada*

ABSTRACT

Evolutionary calculations for stars in close binary systems are in high demand to obtain better constraints on gravitational wave source progenitors, understand transient events from stellar interactions, and more. Modern one-dimensional stellar codes make use of the Roche lobe radius R_L concept in order to treat stars in binary systems. If the stellar companion is approaching its R_L , mass transfer treatment is initiated. However, the effective acceleration also affects the evolution of a star in a close binary system. This is different from the gravity inside a single star, whether that single star is rotating or not. Here, we present numerically obtained tables of properties of stars in a binary system as a function of the effective potential: volume-equivalent radii of the equipotential surfaces, effective accelerations and inverse effective accelerations averaged over the same equipotential surfaces and the properties of the L_1 plane cross-sections. The tables are obtained for binaries where the ratios of the primary star mass to the companion star mass are from 10^{-6} to 10^5 and include equipotential surfaces up to the star's outer Lagrangian point. We describe the numerical methods

used to obtain these quantities and report how we verified the numerical results. We also describe and verify the method to obtain the effective acceleration for non-point mass distributions. We supply a sample code showing how to use our tables to get the average effective accelerations in one-dimensional stellar codes.

Keywords: Multiple star evolution — Binary stars — Roche Lobe — Lagrange points

2.1 Introduction

Binary stars are stellar systems consisting of two stars that are gravitationally bound together and orbiting around each other. If the radius of one of the stars during the course of its evolution becomes comparable to the orbital separation, the binary is termed a close binary. In a close binary such phenomena as tidal spin-up, stable mass transfer (MT), or unstable MT (common envelope evolution) can occur. The evolution of each star in a binary system can be significantly altered from the evolution of a similar but evolved-in-isolation star. Substantial attention is now given in modern one-dimensional (1D) stellar codes to treat the evolution of stars on their way toward the start of MT. The structure of the donor star, specifically of its envelope, at the start of MT – when the volume of the donor star is approaching the volume of its Roche lobe – plays a crucial role in determining whether the MT proceeds stably or unstably.

Upon approaching contact, each star in a binary system is affected strongly by the gravitational field of its companion and by the binary’s orbital motion. However, the primary effect that is considered by 1D stellar evolutionary codes is the size of the Roche lobe of the donor star. Recently, it has become appreciated that the donor star may remain in a state of substantial Roche lobe overflow (RLOF)¹ for an evolutionary-noticeable time while keeping MT in a stable regime, appearing, for example, as

¹As substantial RLOF, we mean an overflow by 10-20 percent of the donor Roche lobe radius, where the donor is approaching the effective potential surface passing through by the donor’s outer Lagrangian point.

Ultra-Luminous X-ray sources [29]. Furthermore, the binding energy of the donor's envelope at the onset of CE, following the MT while the donor significantly overfills its Roche lobe, plays an essential role in the initial conditions of three-dimensional (3D) simulations of common envelope events [24]. When a star is close to its Roche lobe radius, or overfills it, the outer parts of the stellar envelope are strongly affected by the effective acceleration in a binary system, and this effective acceleration is different from the one that a single star experiences. While the knowledge of what is happening to the star in this regime has been around for about 60 years[30], this physics has not yet been included in detail in 1D stellar calculations.

The main goal of this paper is to provide the community with the database we have constructed. That database contains the various properties of binary stellar systems and the code that allows anyone to easily use binary physics in their future binary or MT numerical studies using 1D codes. We review in § 2 the physics that becomes relevant when simulating the gravitational field of a binary star. In § 3 we discuss the assumptions made to approximate binary stars into a 1D scheme, and the numerical methods employed to obtain volume-equivalent radii and average gravitational accelerations for our tables; we also obtain some analytical expressions which determine how this gravitational acceleration behaves close to the center of the donor star, and allow verification of the numerical method in this regime. In § 4 we verify our results by comparing them to various published results and present self-convergence checks. In § 5 we discuss the effects of a non-point mass on the binary potentials, and how to use our tables in the case of non-point masses. This Paper I is devoted to the numerical methods only. The application of the tables that we obtain for binary evolution, and the scientific outcomes, are described in the follow-up Paper II.

2.2 Binary in a corotating frame

Here we review the theory of binary's effective potential and introduce the specific quantities we obtain numerically and present in the database.

2.2.1 Effective binary potential.

We consider a coordinate system in corotation with the binary, with the origin at the donor star's center. The xy plane is the plane of the orbit, and the co-rotating plane is rotating around the axis which passes through the center of mass of the binary system. The effective potential Ψ is then

$$\Psi(X, Y, Z) = -\frac{GM_1}{|R_1|} - \frac{GM_2}{|R_2|} - \frac{1}{2}\Omega^2 \left[\left(X - a\frac{M_2}{M_1 + M_2} \right)^2 + Y^2 \right], \quad (2.1)$$

where M_1 and M_2 are the donor and companion star masses, a is the orbital separation, $\Omega = \sqrt{G(M_1 + M_2)/a^3}$ is the binary system's orbital angular velocity, and R_1 and R_2 are the distances of each element to the donor star's and companion star's centers,

$$\begin{aligned} |R_1| &= \sqrt{X^2 + Y^2 + Z^2}, \\ |R_2| &= \sqrt{(X - a)^2 + Y^2 + Z^2}. \end{aligned} \quad (2.2)$$

We construct a unitless (or scaled) potential ξ following the convention of [18],

$$\Psi \equiv -\frac{G(M_1 + M_2)}{2a} \xi. \quad (2.3)$$

We introduce the mass ratio q

$$q \equiv \frac{M_1}{M_2}, \quad (2.4)$$

and unitless distances

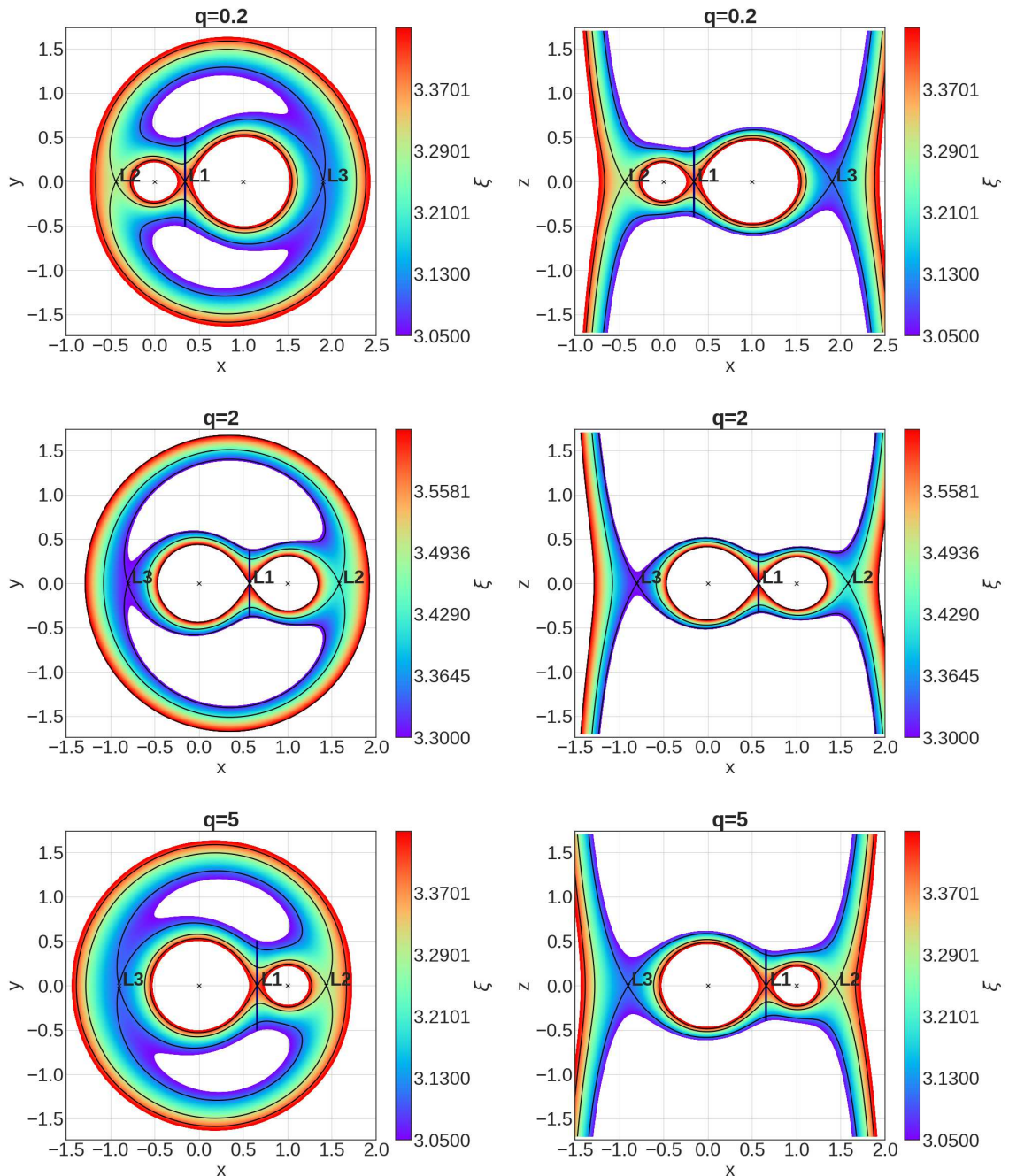


Figure 2.1: Two-dimensional slices showing the scaled potential ξ in a binary corotating frame for three mass ratios: $q = 0.2, 2,$ and 5 , from top to bottom. Shown are slices in the xy -plane (left panels) and xz -plane (right panels). The color bar represents the chosen range of the scaled potential ξ at each point. We plot a narrow range of equipotentials for a better resolution in the region of interest; the white areas are where ξ is outside the chosen ranges. The coordinates are in units of the orbital separation, and the Lagrange points have been denoted by L_i . The black line passing through L_1 is the L_1 -plane (the plane through the first Lagrange point and perpendicular to the line attaching the two stars). The equipotential surfaces passing through $L_1, L_2,$ and L_3 are shown with black lines.

$$x \equiv \frac{X}{a}, \quad y \equiv \frac{Y}{a}, \quad z \equiv \frac{Z}{a}, \quad |r_1| \equiv \frac{|R_1|}{a}, \quad |r_2| \equiv \frac{|R_2|}{a}. \quad (2.5)$$

Then ξ can be written as

$$\begin{aligned} \xi(x, y, z) = & \frac{q}{(1+q)} \frac{2}{|r_1|} + \frac{1}{1+q} \frac{2}{|r_2|} \\ & + \left[\left(x - \frac{1}{1+q} \right)^2 + y^2 \right]. \end{aligned} \quad (2.6)$$

Example contour plots of the unitless equipotentials for several mass ratios (two-dimensional slices for xy plane and xz plane) are shown in Figure 2.1. In the case of a binary considered in a corotating frame, five equilibrium points exist that correspond to local extrema of the effective potential. The most important for studies of binary interactions are the positions of unstable equilibrium L_1 , L_2 , and L_3 , located on the line through the centers of the two large bodies (see examples shown in Figure 2.1). In this paper, we will refer to L_1 as the inner Lagrangian point and L_2 and L_3 as the outer Lagrangian points. The outer Lagrangian point closest to the donor star is L_2 for $q < 1$, and is L_3 for $q > 1$.

2.2.2 Effective acceleration.

We are interested in finding the unitless effective acceleration η , acting in the direction normal to the equipotential surfaces. This is the gradient of the potential, which is perpendicular to the equipotential surface at each point,

$$\eta = -\nabla\xi. \quad (2.7)$$

It is easiest to find this gradient of the potential by using its x , y , and z components, η_x , η_y , and η_z , respectively,

$$\eta_x = \frac{2q}{1+q} \frac{x |r_1|}{r_1^4} + \frac{2}{1+q} \frac{(x-1) |r_2|}{r_2^4} - 2 \left[x - \frac{1}{1+q} \right], \quad (2.8)$$

$$\eta_y = \frac{2q}{1+q} \frac{y |r_1|}{r_1^4} + \frac{2}{1+q} \frac{y |r_2|}{r_2^4} - 2y, \quad (2.9)$$

$$\eta_z = \frac{2q}{1+q} \frac{z |r_1|}{r_1^4} + \frac{2}{1+q} \frac{z |r_2|}{r_2^4}. \quad (2.10)$$

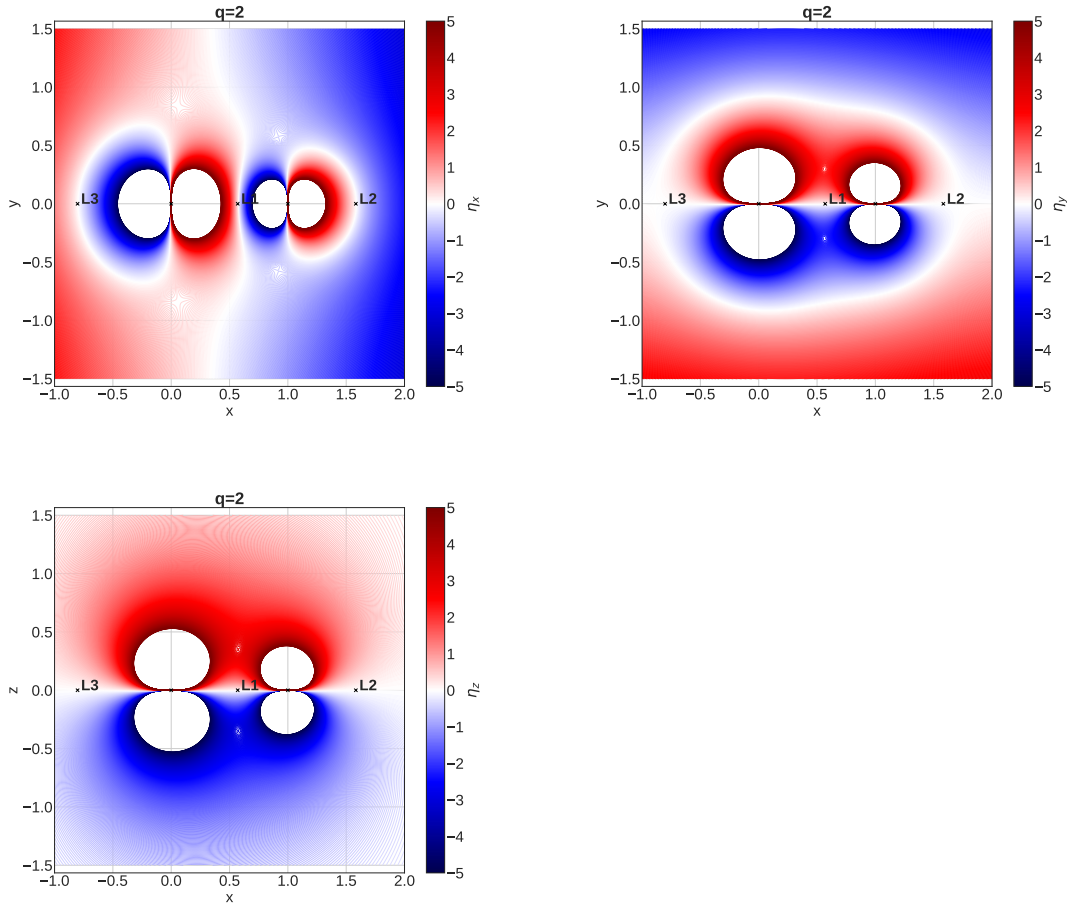


Figure 2.2: η_x , η_y , and η_z shown for mass ratio $q = 2$. The coordinates are in units of the orbital separation.

A plot depicting η_x , η_y , and η_z can be seen in Figure 2.2. The unitless effective acceleration η is then given by

$$\eta = \sqrt{\eta_x^2 + \eta_y^2 + \eta_z^2}. \quad (2.11)$$

Contours for effective accelerations are shown in Figure 2.3. The effective acceleration with physical units $g_{\text{eff}} =$ can be then recovered as:

$$g_{\text{eff}} = \frac{G(M_1 + M_2)}{2a^2}\eta. \quad (2.12)$$

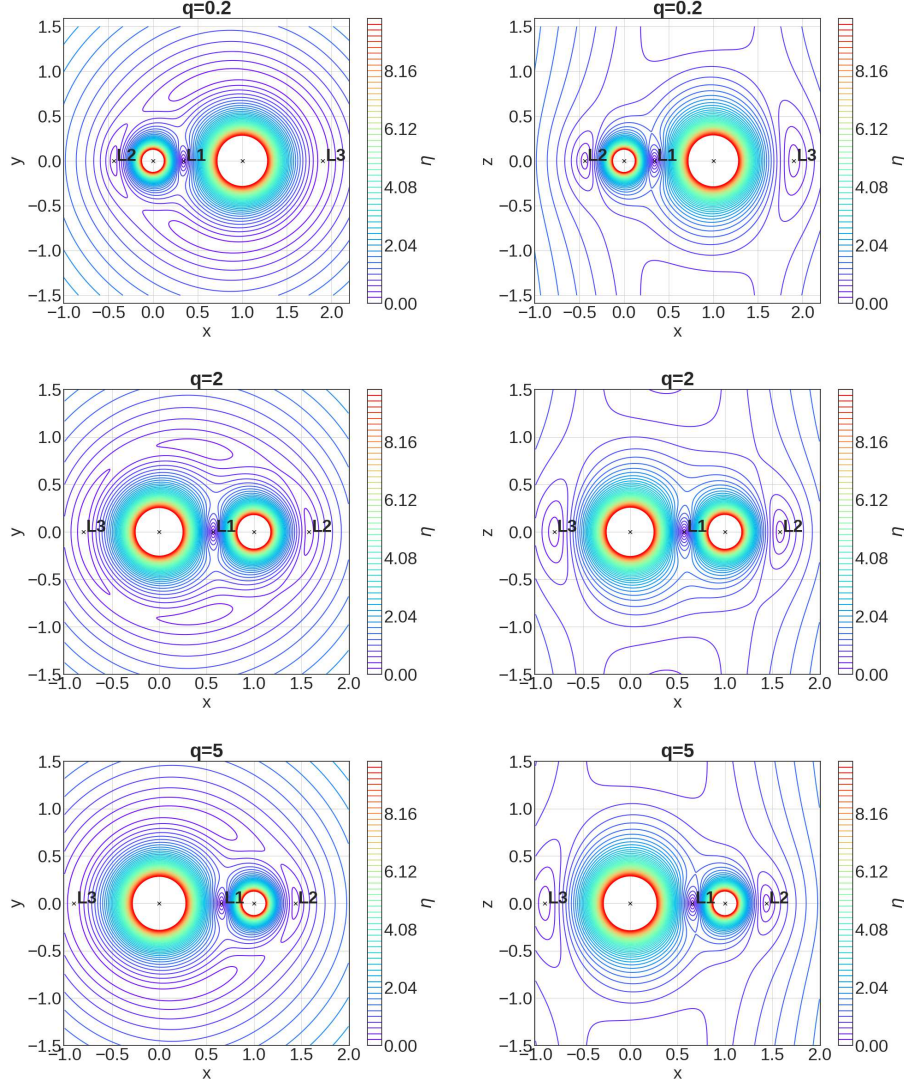


Figure 2.3: Two-dimensional slices showing the contours of the effective acceleration η , in a binary corotating frame, for three mass ratios: $q = 0.2, 2,$ and 5 , from top to bottom. Shown are slices in the xy -plane (left panels) and xz -plane(right panels). The coordinates are in units of the binary separation, and the Lagrange points have been denoted by Li .

2.3 One-dimensional representation

As shown in Figures 2.1 and 2.3, for stars in a binary system, there is no spherical symmetry for either effective potentials nor effective accelerations. Close to the center of each star, a close-to-spherical symmetry can be observed, but the further away from the center of each star one goes, the more significant the influence of its companion and of the orbital motion becomes. The closer one gets to the L_1 point, the more the shape of the potential gets close to a teardrop shape. Outside of the L_1 point, the equipotentials take on a shape similar to a peanut. The effective acceleration, on the other hand, entirely disappears at L_1 .

Our goal here is to develop a method to approximate 3D binary stars' gravitational fields for 1D considerations. Our approach is based on the concept of equipotential shells (3D shells that enclose the center of the stars). We will only focus on the donor star for the remainder of the paper. A 3D depiction of a sample equipotential shell outside of the Roche lobe and limited by the L_1 -plane can be seen in Figure 2.4. The L_1 -plane is the plane that is parallel to the $y - z$ plane, and passes through the L_1 point.

The key physical property of the equipotential shells is that, in the case of hydrostatic equilibrium, both isobaric surfaces and surfaces of constant density coincide with equipotential surfaces. Therefore here we consider averaging the effective acceleration that affects the star over the equipotential surfaces. The effective accelerations are found as a function of the volume-equivalent radii of the same equipotential surfaces.

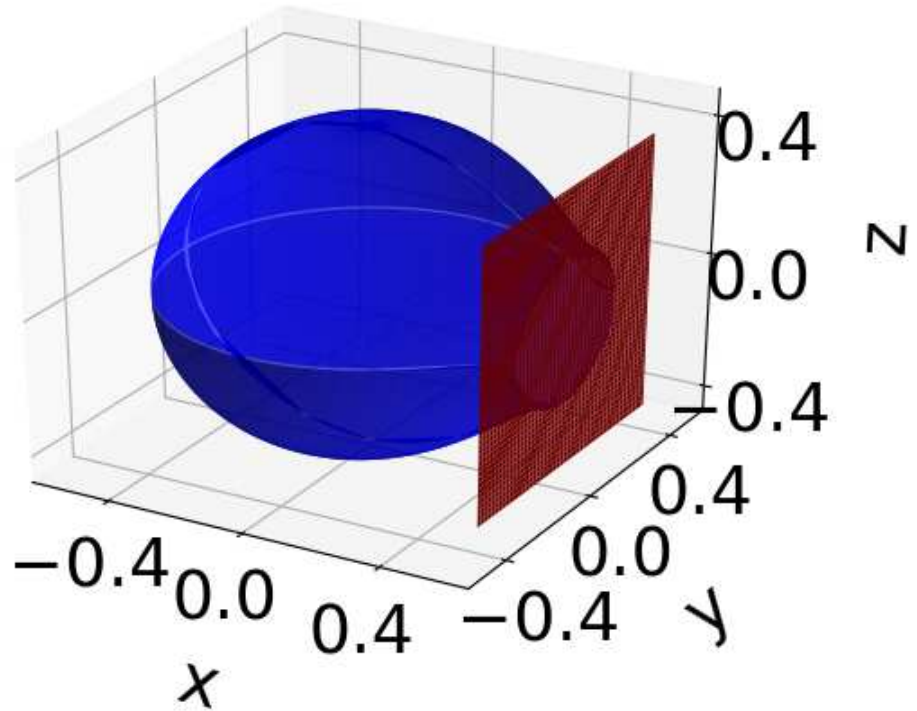


Figure 2.4: A sample equipotential surface outside of the Roche lobe in a binary star with the mass ratio $q = 2$, shown in blue color. The equipotential surface is limited by the L_1 -plane, shown in red color. The coordinates are in units of the orbital separation.

2.3.1 Volume-equivalent radii

Each equipotential surface encloses some volume V_{equip} . This volume can be associated with a sphere of the same volume. This sphere has a so-called volume-equivalent radius

$$R_{\text{eq}} = \sqrt[3]{\frac{3V_{\text{equip}}}{4\pi}}. \quad (2.13)$$

The idea of the volume-equivalent radius was introduced in the past (see, for example, [30]). The best known numerical fitting of 3D integrations for the unitless volume-equivalent Roche-lobe radius is the famous equation of [19]

$$r_{L_1} = \frac{0.49q^{2/3}}{0.6q^{2/3} + \ln(1 + q^{1/3})} . \quad (2.14)$$

The physical volume-equivalent Roche lobe radius of the star R_{L_1} then is found by multiplying r_{L_1} by the orbital separation a , $R_{L_1} = r_{L_1}a$.

For volume integrations, we use spherical coordinates. We define i and j as the indices describing the directions in φ (azimuthal angle) and ϑ (polar angle) for integrations, where $\varphi \in [0, \pi]$ and $\vartheta \in [0, \pi/2]^2$. We divide each of these domains into n_φ and n_ϑ respectively (we adopt $n_\varphi = 2n_\vartheta$). We define k to be the index describing the potential shell with ξ_k . The r_{ijk} is the location of the equipotential shell ξ_k in each angular direction ij , or, specifically, the distance to the origin r for the given angles φ and ϑ . r_{ijk} is found iteratively until at least the convergence condition

$$\left| \frac{\xi(r_{ijk}, \varphi_i, \vartheta_j) - \xi_k}{\xi_k} \right| \leq 10^{-12} \quad (2.15)$$

is satisfied. Here $\xi(r, \varphi, \vartheta)$ is the potential at the location (r, φ, ϑ) , while ξ_k is the potential for the equipotential surface for which we search.

The numerical integrator uses spherical volume elements in each angular direction φ and ϑ , and the volume between the k_{th} shell and $(k - 1)_{th}$ shell in the potential is

$$\Delta V_{\text{sph},k} = r_{ijk}^2 \sin \vartheta_j \Delta r_{ijk} \Delta \varphi \Delta \vartheta . \quad (2.16)$$

Δr_{ijk} is the step in the ij direction. This is not constant for the entire potential shell k but depends on the location of the currently sought potential ξ_k in ij -direction, and the location of the previous potential, ξ_{k-1} . Using the symmetry of the equipotential in a binary system, we perform the volume integration in the angular domain as above and then multiply by 4.

²The values of unitless acceleration, η , and equipotentials, ξ , in a binary system have the symmetry along z -direction with respect to the orbital plane xy , as well as along y -direction with respect to xz -plane. Therefore, only integrations in $\varphi \in [0, \pi]$ and $\vartheta \in [0, \pi/2]$ are needed.

The volume integrations are limited by the outer Lagrange point’s equipotential shell of the donor star, and the L_1 plane. These limitations affect volume integrations for shells that are located outside the L_1 equipotential. The L_1 plane is depicted as a black line in the 2D slice of Figure 2.1 and as a red plane in the 3D Figure 2.4.

2.3.2 Effective accelerations

The unitless effective accelerations at each location are found using equations 2.8, 2.9, and 2.10.

The weighted averages of the effective acceleration for each equipotential shell are obtained with the area of the triangular elements on that equipotential surface dA_{ij} ³,

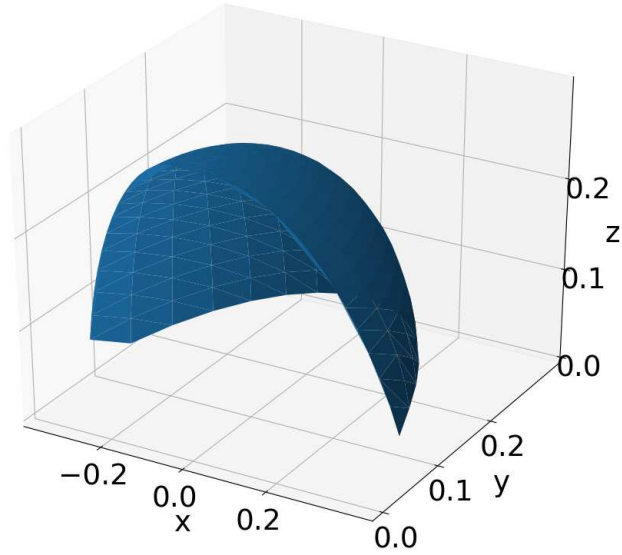


Figure 2.5: A depiction of a part of the equipotential shell with triangular meshes on it shown in 3D; for a random shell in the case of the mass ratio $q = 0.5$. Only a part of the integration domain is shown, to make the triangular mesh visible.

³We compared the performance of triangular mesh area elements and spherical area elements (as did [18]) and found that the triangle method provides faster convergence to obtain surfaces on equipotential shells. This is especially important for the shells outside the Roche lobe, where element areas of the surfaces of equipotentials do not resemble spherical area elements.

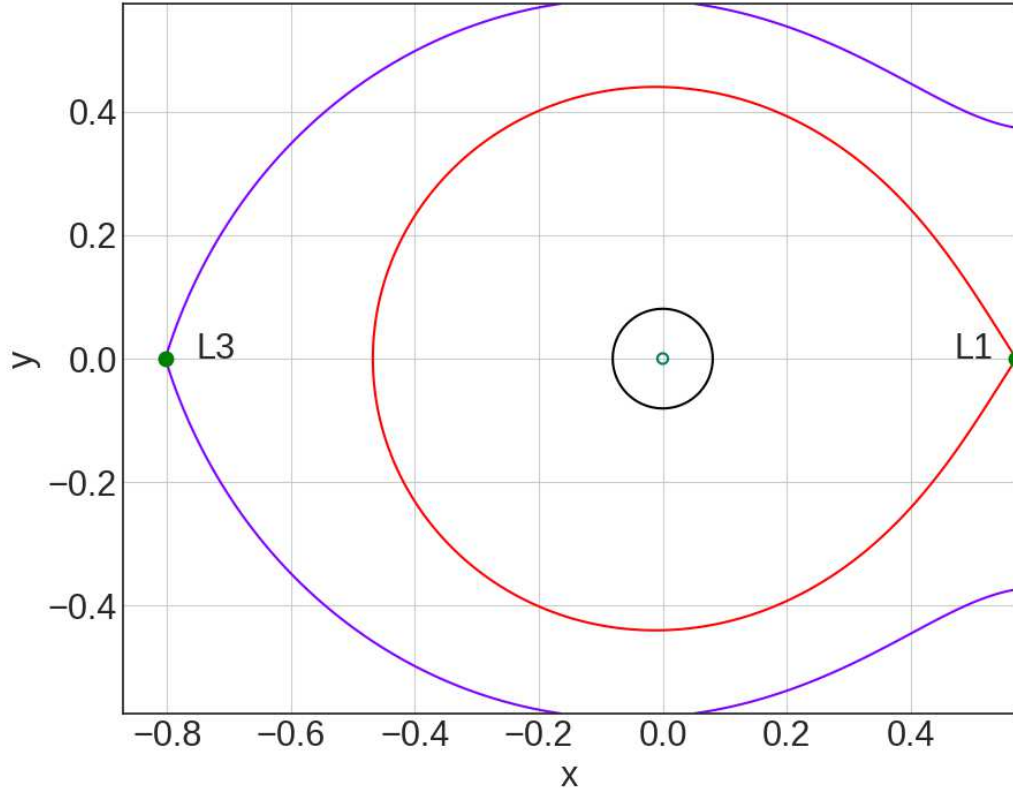


Figure 2.6: The three zones of integration; this specific example is for a mass ratio of $q = 2$. The zones are defined as described in equation 2.19, see § 3.3 for further details.

$$\eta_{\text{avg}} = \frac{\sum_i \sum_j \eta_{ij} dA_{ij}}{\sum_i \sum_j dA_{ij}}, \quad (2.17)$$

where i and j are the indices of φ and ϑ for which the triangles are summed. Here η_{ij} is the unitless effective acceleration averaged over three triangles' vertices.

Figure 2.5 shows a sample triangular mesh scheme for an equipotential shell.

2.3.3 Integration zones

The potential is very sensitive to the distance from the center. To accommodate this sensitivity, we divide the integration zones into three regions:

$$\xi_1 = \xi(0, 0, 0, q) \tag{2.18}$$

$$\xi_2 = \xi(0.05x_{L_1}, 0, 0, q)$$

$$\xi_3 = \xi(x_{L_1}, 0, 0, q)$$

$$\xi_4 = \xi(x_{L,\text{outer}}, 0, 0, q)$$

An example of the three integration regions can be seen in Figure 2.6.

Near the center, the true binary potential and effective acceleration η are not very different from these in a spherically symmetric single star

$$\begin{aligned} \xi &= \xi_{\text{ss}} + \Delta\xi, & \Delta\xi &= \left(\frac{3 + 2q}{2q(1 + q)}r + \frac{2q - 1}{6q}r^3 \right) \xi_{\text{ss}}, \\ \eta &= \eta_{\text{ss}} + \Delta\eta, & \Delta\eta &= -\frac{2(1 + q)}{3} \frac{r^3}{q} \eta_{\text{ss}}. \end{aligned} \tag{2.19}$$

Here ξ_{ss} is the unitless effective binary potential in a a spherically symmetric star, η_{ss} is the unitless effective acceleration in a spherically symmetric star, and r is the unitless distance to the center of the first star (distance in the units of the binary separation). For the derivation, see derivations in Appendix §C and Equation 2.40. The expected deviations near the center, $\Delta\xi$ and $\Delta\eta$, are very small.

The expected local truncation error due to the limited resolution during numerical integration for any quantity is of the order of $2\pi^2/n_\phi^2$ times that quantity. We have checked and verified numerically that our integrations for volume equivalent radii and averaged effective accelerations are limited by the adopted angular resolution, as expected for R_{err} . The limited numerical precision with which we can obtain solutions near the center does not allow us to resolve this behavior correctly, for instance the error in finding volume equivalent radii is $\delta_{\text{err}}(R_{\text{eq}}) \approx (2/3)(\pi^2/n_\phi^2)$ (assuming that R_{eq} is of the order of one). However, this error might be comparable to the radius itself and hence leads to an even larger error in finding the effective gravity. We introduce

as r_{an} the unitless distance to the origin within which the analytical solutions using Equation 2.19 have to be used, as opposed to the distances $r > r_{\text{an}}$, where numerical integrations have to be used.

We have verified that for the mass ratios in the range of $[10^{-6}, 10^5]$, at $r_{\text{an}} = 0.05x_{L_1}$, the non-sphericity effect is $\Delta\xi/\xi_{\text{ss}} \lesssim 10^{-4}$, and hence the higher terms do not contribute substantially. This makes Equation 2.19 directly applicable. The numerical precision to find the potential or the effective acceleration, with $n_\varphi = 4000$, is approximately 10^{-6} . With this resolution, the numerical "noise" due to truncation error contributes at less than a percent of the obtained values for various quantities for our smaller mass ratio $q = 10^{-6}$, and as little as 0.01% for all mass ratios $q > 1$. The numerical noise decreases with r , albeit the role of terms neglected in Equation 2.19 grows. Therefore $r_{\text{an}} = 0.05x_{L_1}$ is a compromise at which we can still trust the analytic solution but can start to trust the numerical solution for a wide range of mass ratios.

For $r < r_{\text{an}}$ we therefore consider that the potential and effective acceleration should be provided by Equation 2.19. For the intermediate zone, we start our numerical integrations at $r = r_{\text{an}}$.

In our runs, we use 500 shells between ξ_2 and ξ_3 , equally spaced in distance between $0.05x_{L_1}$ and x_{L_1} and 100 shells between ξ_3 and ξ_4 , equally spaced in the logarithm of the potential between ξ_{L_1} and $\xi_{L_{\text{outer}}}$.

2.3.4 Properties in the L_1 neighborhood cross-section

We also compute several properties at the L_1 plane to provide in our database. These properties are functions of unitless equipotential shells passing through the L_1 plane. The intersections of equipotential shells with the L_1 plane appear as ellipse-like curves on the L_1 plane (see Figure 2.7). The tabulated properties are as follows⁴:

⁴Note that all L_1 -plane properties are obtained for equipotential shells exceeding the Roche Lobe. In the database we provide, all the columns corresponding to these properties are set to zero for all equipotential shells within the Roche lobe.

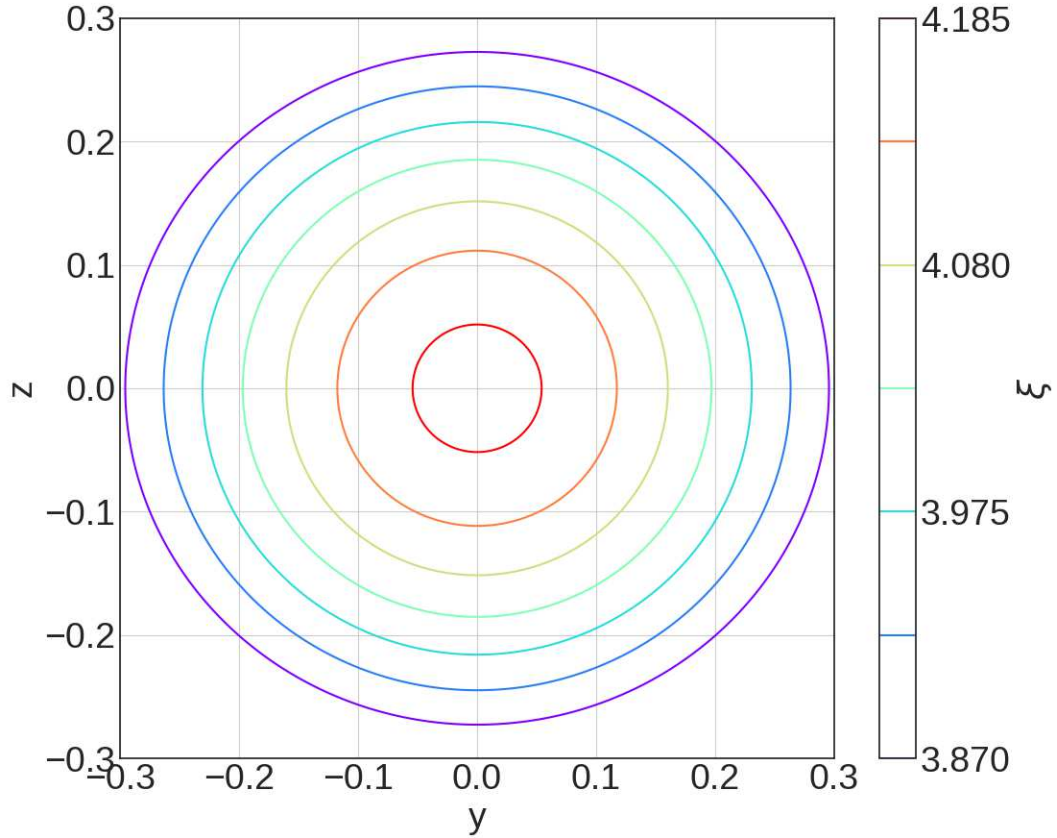


Figure 2.7: The intersection of several equipotential surfaces with the L_1 plane for $q = 0.2$. Axes are in units of the orbital separation.

- The area of the cross-section of the L_1 plane and the equipotential shell passing through it, as a function ξ . The area integration uses polar coordinates with 4000 angular resolution per quadrant
- The locations of intersections of this cross-section with the xy -plane and xz -plane, as a function of ξ .
- The effective acceleration averaged over the intersection between the equipotential and the L_1 - plane.
- The effective acceleration averaged over the entire area of each of these elliptical cross-sections.

2.4 The numerical results

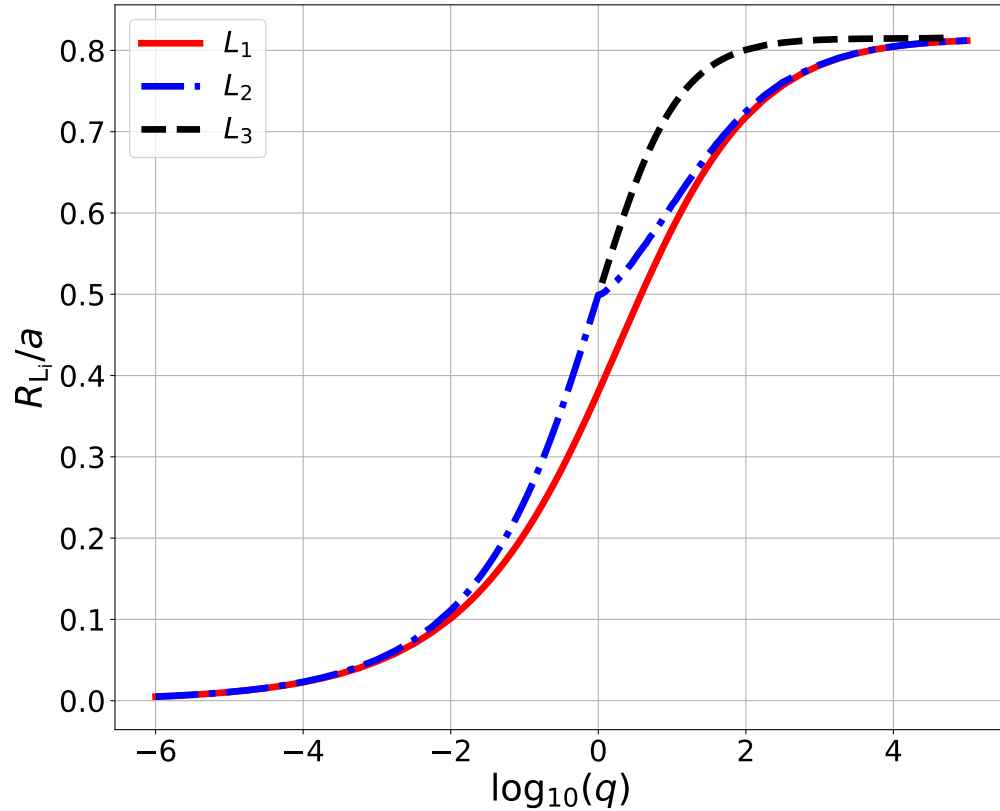


Figure 2.8: This plot shows the results of our highest resolution run for the volume equivalent radii passing the first three Lagrange points, as a function of the mass ratio. The horizontal axis is in the units of orbital separation. R_{L_3} volume around the donor star exists only for mass ratios greater than 1. Note that the outer Lagrange point is L_3 for mass ratios greater than 1, and is L_2 for mass ratios less than 1.

2.4.1 Self-convergence

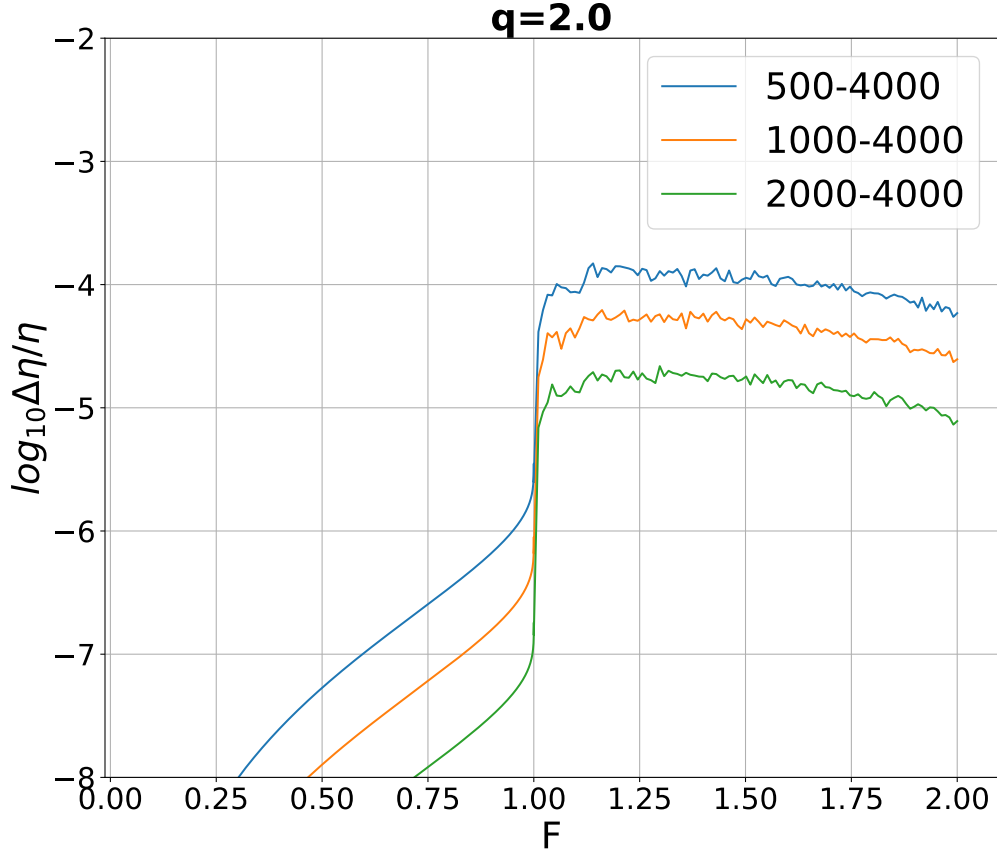


Figure 2.9: Self-convergence test for the effective acceleration for mass ratios $q = 2$. The vertical axis is the normalized error in effective acceleration for angular resolutions $m = 500, 1000, 2000$, and 4000 (Equation 2.20). The horizontal axis is F , the fill-out factor F (Equation 2.21). $F > 1$ means the equipotentials are outside of the Roche lobe.

We have computed the properties of interest for 109 mass ratios in the range of $\log_{10} q \in [-6, 5]$. We have divided this range into three regimes based on the possible applications it could have:

- A** : $\log_{10} q \in [-6, -2], \Delta(\log q) = 0.25$
- B** : $\log_{10} q \in (-2, 2], \Delta(\log q) = 0.05$
- C** : $\log_{10} q \in (2, 5], \Delta(\log q) = 0.25$

The first range **A** is relevant to the regime of planets or stars orbiting a supermassive black hole, range **B** is a typical range of mass ratios for two stars in a binary system, and range **C** could be used in studies where one wants to investigate the effects of the interactions of a star and a Jupiter-like planet, from the star’s perspective. The list of all properties provided for each mass ratio can be found in Appendix A, Table 2.1.

We show the volume equivalent radii passing the first three Lagrange points, as a function of the mass ratio in Figure 2.8.

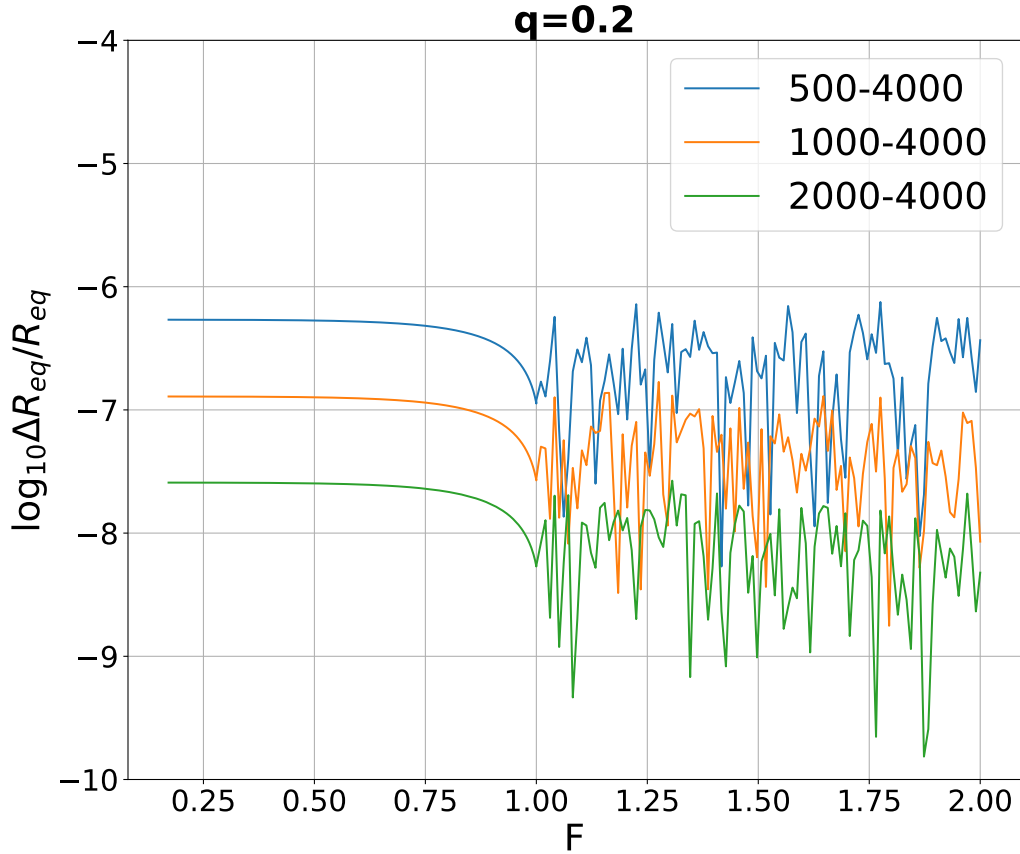


Figure 2.10: Self-convergence test for the volume-equivalent radius for mass ratio $q = 0.2$. The vertical axis is the normalized error in volume equivalent radius at L_1 for angular resolutions $m = 500, 1000, 2000$, and 4000 (Equation 2.20). The horizontal axis is the fill-out factor F (Equation 2.21).

We investigate at which angular resolution our numerical solver self-converges.

Under the self-convergence test, we mean a numerical study in which the resolution of numerical interactions is continuously increased, to see a) if the difference between the numerical outcomes at increasing resolutions continuously decreases, without new features appearing and b) that said difference becomes smaller than the required numerical precision. While self-convergence is often termed as simply convergence, it is important to remember that self-convergence does not verify that the numerical results have converged to a correct solution, for the latter one has to do at least verification tests⁵. The number of angular zones we considered is $\varphi = 500, 1000, 2000,$ and 4000 for φ in the range $\varphi \in [0, \pi]$ and ϑ in $\vartheta \in [0, \pi/2]$.

For a quantity A , obtained with the angular resolution m , we define as the normalized error

$$\frac{\Delta A_m}{A} = \frac{A_m - A_{4000}}{A_{4000}} \quad (2.20)$$

We use the highest angular resolution, $n_\phi = 4000$, to compare the other angular resolutions with it and see whether the deviation is decreasing with increasing angular resolution or not.

In Figures 2.9 and 2.10 we provide typical convergences for effective acceleration and volume equivalent radii as functions of the fill-out function F . F is a unitless function used to compare different mass ratios' potential distributions up to the outer Lagrange points (which could be L_2 or L_3), defined as by [18]:

$$\begin{aligned} F &= \frac{\xi_{L_1}}{\xi}, \text{ for } \xi \geq \xi_{L_1}, \\ F &= 1 + \frac{(\xi_{L_1} - \xi)}{(\xi_{L_1} - \xi_{L_{outer}})}, \text{ for } \xi \leq \xi_{L_1}. \end{aligned} \quad (2.21)$$

F is defined in such a way that $F \in [0, 1]$ for potential shells inside and up to the L_1 equipotential surface, and $F \in [1, 2]$ for shells outside of the L_1 equipotential

⁵Validation – i.e., the measure of numerical model accuracy between model predictions and measurements of the real world – is not possible in our case, as for most astrophysical problems.

and inside the outer Lagrange point's equipotential shell. Our results show that self-convergence is obtained quickly. For all mass ratios, the absolute value of the normalized error for effective accelerations is less than 10^{-4} ($|\Delta A_m/A| < 10^{-4}$) for $m = 4000$ outside of the Roche lobe, and is below 5×10^{-6} within the Roche lobe. Volume-equivalent radii and equipotential areas are obtained with the normalized error less than 10^{-7} . We, therefore, consider our final results presented in the database and obtained with $n_\varphi = 4000$ to be self-converged.

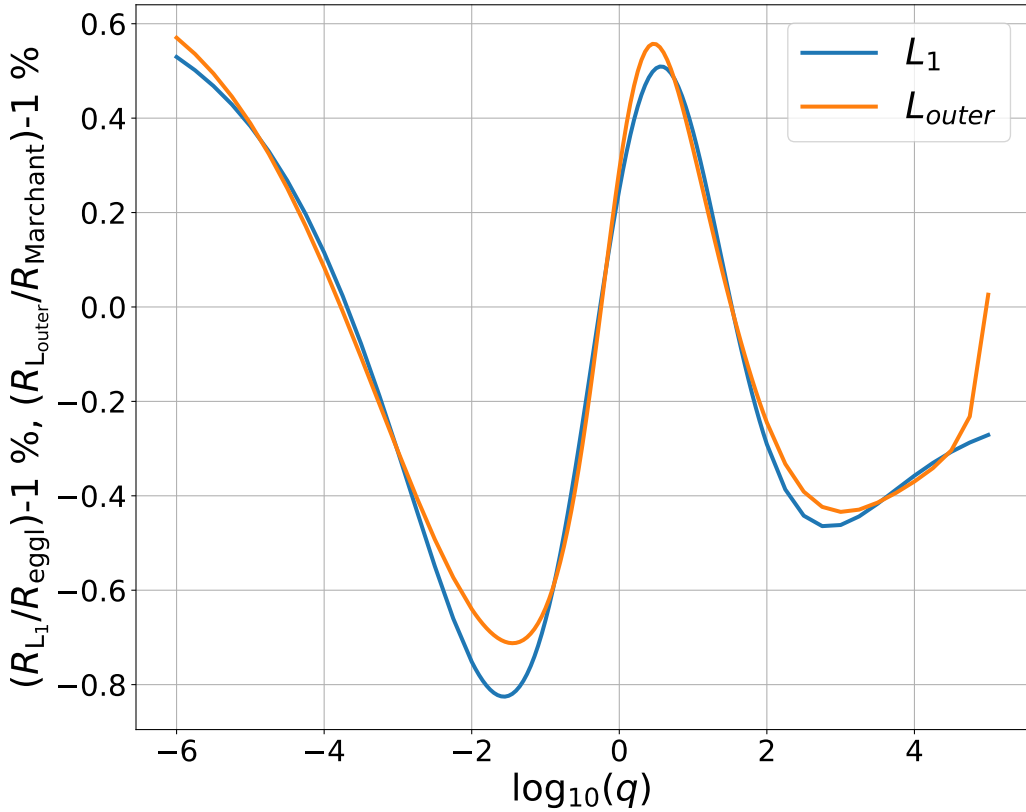


Figure 2.11: Deviation of R_{L_1} (L_1 volume-equivalent radius) from [19] relation (the blue line). Deviation of R_{outer} (the outer Lagrange equipotential volume-equivalent radius) from the one provided by the Equation 2.22 (the orange line). The deviations are shown as functions of mass ratio q .

2.4.2 Verification for Volume-Equivalent Radii

We have verified our volume-equivalent radii against two numerical fits available in the literature (i) the L_1 equipotential ([19] see also Equation 2.14 in this paper), and (ii) the outer Lagrange point's equipotential as provided by [31],

$$\frac{R_{\text{outer}}}{R_{L_1}} = 1 + \frac{2.74}{1 + [(1.02 - \ln q)/\sigma]^2} \frac{1}{7.13 + q^{0.386}} ,$$

and

$$\sigma = \frac{49.4}{12.2 + q^{-0.208}} . \tag{2.22}$$

In the above, R_{L_1} is the radius of the Roche lobe found by using the approximation of [19]. Note that here we modified Equation (3) of [31] to match our definition of q ([31] define the mass ratio as the companion star's mass divided by the donor's).

The results are shown in Figure 2.11. The fitting equation for R_{L_1} of [19] has been reported (in the paper where the equation was presented) to be accurate to 1%. The fitting equation for R_{outer} by [31] has been reported by them to be accurate to 0.15%. However, the equation for R_{outer} also, by definition, includes the uncertainty in R_{L_1} from the formula of [19]. We find that we have agreement within 1% for both fitting equations.

2.4.3 Verification for Effective Acceleration

[18] has provided coarse tables with numerically obtained average effective acceleration on the equipotential as a function of the potential. We have compared our average effective acceleration passing the L_1 shell and the L_2 shell (obtained with $n_\varphi = 4000$) with that of [18]. The deviations are within 10^{-4} for the values at the outer Lagrangian equipotential (their $F = 2$), and within the last significant digit of the values that [18] provides for L_1 equipotential (their $F = 1$). These deviations are consistent with our test for self-convergence.

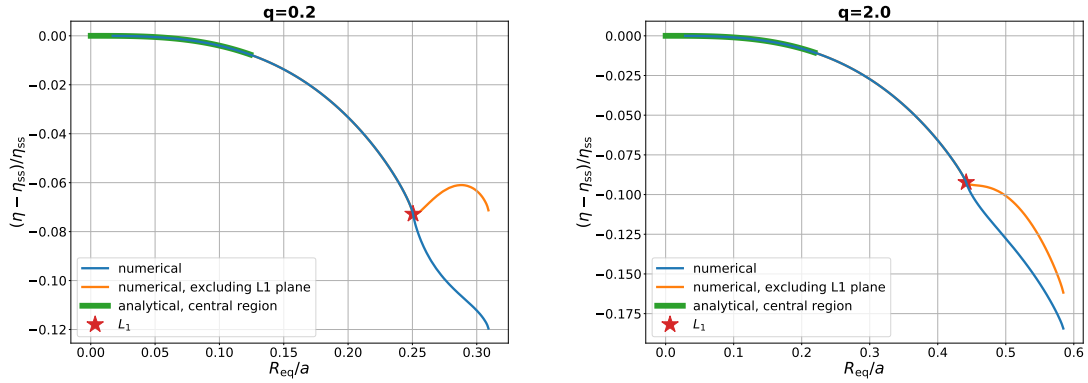


Figure 2.12: The deviation in effective acceleration from our tables for mass ratios $q = 0.2$ (the left plane) and $q = 2$ (the right plane), as a function of the volume equivalent radius. The red star denotes the equipotential passing L_1 . The green curve in each figure is the analytical expression 2.40. We show the analytical solution for the distances within 0.5 of R_{L_1} , albeit we use it only for the distances within 0.05 of x_{L_1} , as described in the text. One can see that the analytical solution matches the numerical solution for a large range of distances. The blue line shows the case when the effective acceleration is average over the whole contour surrounding the star, and the orange line shows the effective acceleration with L_1 plane is excluded from the averaging.

2.4.4 Deviation of the binary effective acceleration from spherically symmetric gravitational acceleration

The final result of the effective acceleration is shown in Figure 2.12. The analytical solution at distances close to the center has also been plotted and, as one can see, the numerical results correspond to the analytical equation very closely.

2.4.5 Deviation of the binary effective acceleration from the case of a solid body rotating star

If a star is a solid body rotator, it experiences an additional acceleration that opposes gravitational acceleration. If one assumes spherical symmetry, the effective acceleration, averaged over a spherical shell, can be expressed in the units of acceleration in a non-rotating star as

$$\frac{\eta_{\text{rot}}}{\eta_{\text{ss}}} = 1 - \frac{2}{3} \frac{1+q}{q} r^3 = 1 + \delta\eta_{\text{rot}} . \quad (2.23)$$

Here we introduced the relative deviation that rotation causes, $\delta\eta_{\text{rot}}$. Analogously, one can consider that our numerically obtained and tabulated acceleration is

$$\frac{\eta}{\eta_{\text{ss}}} = 1 + \delta\eta_{\text{tab}} . \quad (2.24)$$

In Figure 2.13, we compare those two terms for the binaries with the mass ratios range in the interests of stellar binaries. The comparison is provided for stars presumed to fill their Roche lobe – their radii are taken to be equal to their volume-equivalent Roche lobe radii. The effective binary potential always results in the average effective acceleration being smaller (in its absolute value) than in the case of a spherically symmetric star that rotates with an angular velocity equal to the binary angular velocity.

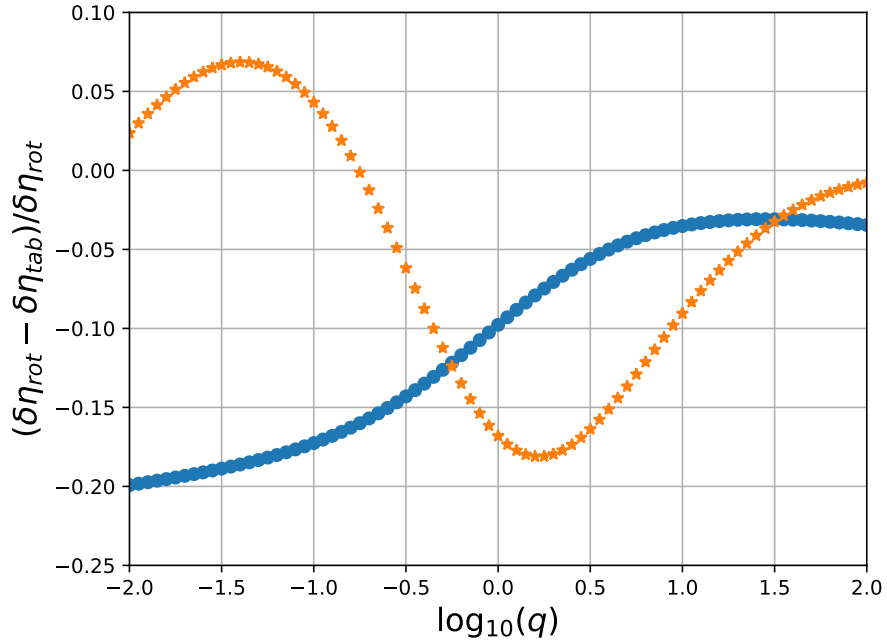


Figure 2.13: The deviation in effective acceleration from our tables from a solid body rotating star, as a function of the mass ratios (blue circles). The deviation is provided for stars that fill their Roche lobe. With orange stars, we show the deviation where we used Eggleton’s equation for Roche lobe radius instead of our integrated quantities for the spherically symmetric acceleration and the rotating term. See §2.4.5.

2.4.6 Alternative treatment of the effective acceleration

It has been argued that instead of the effective gravity g (averaged over the equipotential), the quantity that should be averaged on the equipotentials for the inclusion in the stellar equations is $\langle g^{-1} \rangle$, (see [32]; [33], [34], for how to use it). We provide the unitless quantity $\langle g^{-1} \rangle$ in our numerical tables. The quantity $\langle g^{-1} \rangle^{-1}$ deviates from spherically symmetric gravity even more significant than $\langle g \rangle$, as can be seen from Figure 2.14 where we show the values on L_1 equipotential for a range of mass ratios $\langle g \rangle \times \langle g^{-1} \rangle = \langle \eta \rangle \times \langle \eta^{-1} \rangle$.

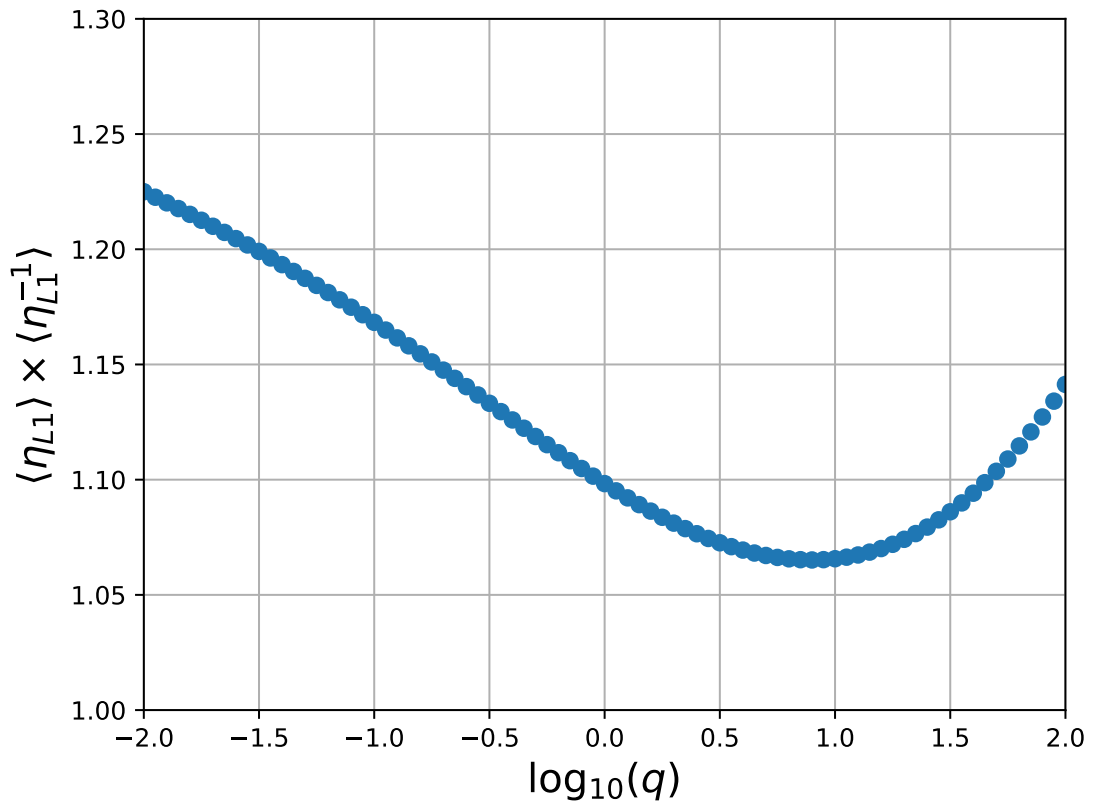


Figure 2.14: The effective gravity averaged over equipotential multiplied by the inverse effective gravity averaged over equipotential, as a function of the mass ratios. See §2.4.6.

2.4.7 How to use the provided quantities

This work is devoted to the evolution of stars within the gravity field of a binary system. Hence, throughout this paper, we use the same definition of the effective acceleration as per Equation 2.11 – we always consider the magnitude of the effective acceleration vector component that is normal to the equipotential surface at each considered location. The adopted definition of the effective acceleration holds for values obtained on the L_1 plane, including the inverse values of the effective acceleration. In the main data table (see Appendix 2.6 for more detail), we provide:

- (a) values from 3D integrations made throughout the closed 3D surface (including the L_1 -plane)
- (b) values from 2D integrations for the L_1 plane only.

When the considered star overfills its Roche lobe, the values on the truncated (limited by the L_1 -plane) equipotential layers of the star are to be reconstructed from the 3D values provided in a), excluding the 2D values provided in b). For example, the effective acceleration at i -equipotential shell inside the star is to be found using the 3D area A , the averaged (over A) 3D effective acceleration η , the 2D area of L_1 -plane $A_{L_{pl}}$, and the averaged (over the L_1 -plane) effective acceleration $\eta_{L_{pl}}$:

$$\eta_i = \frac{\eta A - \eta_{L_{pl}} A_{L_{pl}}}{A - A_{L_{pl}}} . \quad (2.25)$$

We also provide the auxiliary data table with values from 3D integrations made throughout the truncated surface only, excluding the L_1 -plane. This table can be used directly without reconstruction. Note that the angle-distributed mesh does not always fall on the cross-section of the 3D equipotential lines and the L_1 -plane. Hence, the truncated 3D area will not have a continuous transition to the L_1 -plane. This 3D integration is prone to carry errors due to an incomplete layer of triangular mesh between 3D equipotential and flat L_1 -plane. While both methods provide essentially

the same value, the second has a more significant numerical convergence error, and we strongly recommend using the reconstruction method.

For the L_1 -plane, the quantities in the main data table are not related to the component of the effective acceleration that is perpendicular to the L_1 -plane, $\eta_{x,L1}$. Suppose one needs values for the x -component of the acceleration only, that can be easily obtained doing 2D integration on the L_1 -plane for η_x with $x = x_{L1}$ (see Equation 2.8), and then recovering the value with physical units by multiplying it by $-G(M_1 + M_2)/2a^2$. While this quantity is not the primary goal of this work, we supplement the averaged values for the η_x -component separately in another auxiliary data table (see Appendix 2.6).

2.5 Effects of a non-point mass

A real star is not a point mass. One has to obtain a 3D stellar model to include the effect of a realistic 3D mass distribution on the effective acceleration. Here, we only consider a first-order effect. We start with defining the local mass fraction as a function of the distance to the center of the first star

$$q_{\text{loc}}(r_{\text{eq}}) \equiv \frac{M_{\text{loc}}(r_{\text{eq}})}{M_2}, \quad (2.26)$$

where $q_{\text{loc}}(r_{\text{eq}})$ is the mass fraction that assumes the mass within the volume-equivalent radius, $M_{\text{loc}}(r_{\text{eq}})$ is the local mass coordinate inside the donor, $M_{\text{loc}}(r_{\text{eq}}) \leq M_1$.

We start by considering the deviation in the gravitational potential due to a non-point mass distribution inside the first star, keeping the second star's gravitational contribution, and the effect from being in the corotating frame, the same as previously

$$\begin{aligned} \psi(\vec{R}) = & -G \int_{M_1} \frac{dm}{|R_1|} - \frac{GM_2}{|R_2|} \\ & - \frac{1}{2} \Omega^2 \left[\left(x - \frac{aM_2}{M_1 + M_2} \right)^2 + y^2 \right] \end{aligned} \quad (2.27)$$

Here, the first term is, in principle, a 3D integral that has to be taken through the donor star's interior. The effective acceleration is the gradient of the effective potential. We consider the changes in the first term of the effective potential due to the mass having a spherically symmetric but non-point mass distribution. The former assumption takes us to the Newton shell theorem, which states that the gravitational field due to the mass inside a given radius acts as a point mass to elements at that radius, whereas the mass outside of that radius does not exert a net gravitational force on those elements. In the case of spherically-symmetric mass distributions, the unitless effective acceleration can be written then as

$$\begin{aligned}
\eta_{x,\text{loc}}(x, y, z) &= \frac{2xq_{\text{loc}}(r_{\text{eq}})}{(1+q)|r_1|^3} + \frac{2(x-1)}{(1+q)|r_2|^3} \\
&\quad - 2\left(x - \frac{1}{1+q}\right), \\
\eta_{y,\text{loc}}(x, y, z) &= \frac{2yq_{\text{loc}}(r_{\text{eq}})}{(1+q)|r_1|^3} + \frac{2y}{(1+q)|r_2|^3} - 2y, \\
\eta_{z,\text{loc}}(x, y, z) &= \frac{2zq_{\text{loc}}(r_{\text{eq}})}{(1+q)|r_1|^3} + \frac{2z}{(1+q)|r_2|^3}.
\end{aligned} \tag{2.28}$$

The total acceleration at the given location can be found as

$$\eta_{\text{loc}}(r) = \sqrt{\eta_{x,\text{loc}}^2 + \eta_{y,\text{loc}}^2 + \eta_{z,\text{loc}}^2}. \tag{2.29}$$

Based on the shape of the local potential, we consider the correctional term for the effective acceleration as

$$\delta\eta(q_{\text{loc}}(r_{\text{eq}}), q, r_{\text{eq}}) = \frac{2(q_{\text{loc}}(r_{\text{eq}}) - q)}{(1+q)} \frac{1}{r_1^2}. \tag{2.30}$$

We also introduce a simple "modified" effective acceleration as

$$\eta_{\text{mod}}(q_{\text{loc}}(r_{\text{eq}}), q, r_{\text{eq}}) = \eta(q, r_{\text{eq}}) + \delta\eta(q_{\text{loc}}(r_{\text{eq}}), q, r_{\text{eq}}). \tag{2.31}$$

Here, $\eta(q, r_{\text{eq}})$ is the same unitless effective acceleration as previously, for point-mass binaries, and its values for each q and r_{eq} can be found from the tables we obtained and provided for the reader.

In order to test this approximation, we considered polytropes with $n = 1.5$ and $n = 3$. For the local mass ratio, we assumed that the mass within each volume-equivalent of the numerically obtained binary equipotential (each equipotential itself is a function of the local mass) is the same as within the same volume in a spherically symmetric polytrope.

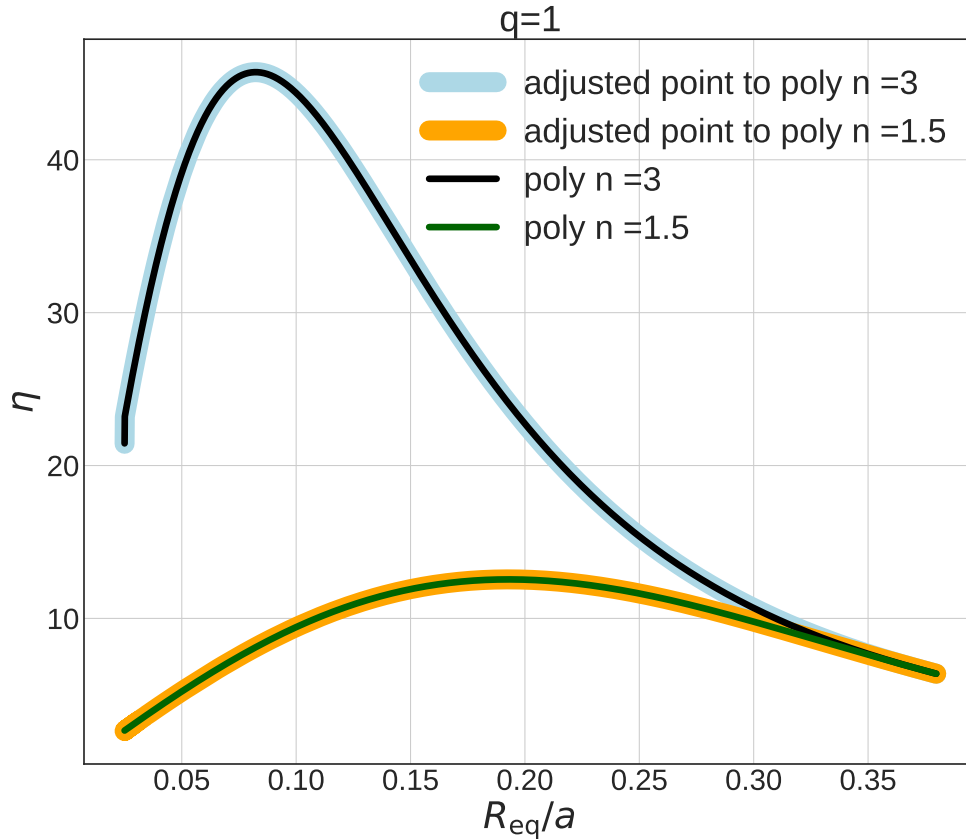


Figure 2.15: The simplified effective acceleration and the integrated effective acceleration, as a function of R_{eq} , for polytropes with $n = 3$ (blue line) and $n = 1.5$ (orange line). Shown for the case $q = 1$.

As shown in Figure 2.15, the exact integration and the simplified method are in agreement with each other. We conclude that the simplified method, as described, can be used to obtain effective accelerations inside the star from our precalculated tables for point mass cases and the correction term. It should be noted that, for

regions close to the center, $r_1 \leq 0.05x_{L_1}$, we make use of the following analytical expression, to obtain the effective acceleration:

$$\eta = \eta_{\text{ss,loc}} + \Delta\eta_{\text{loc}}; \quad \Delta\eta_{\text{loc}} = -\frac{2(1+q)}{3q_{\text{loc}}(r_1)}r_1^3\eta_{\text{ss,loc}}. \quad (2.32)$$

It is assumed that, in the vicinity of the center, $r_{\text{eq}} \simeq r_1$. In this equation, $\eta_{\text{ss,loc}}$ is the effective acceleration of a single, non-point mass star up to that zone:

$$\eta_{\text{ss,loc}} = \frac{2q_{\text{loc}}(r_1)}{(1+q)}\frac{1}{r_1^2}. \quad (2.33)$$

The derivation of these equations is written in C.3.

The subroutine that we provide (see the description in Appendix B) makes use of the described method.

2.6 Conclusions

We have described the method we use to obtain numerically effective accelerations for a star in a binary system as a function of either the effective potential, or the volume-equivalent radius.

Our method is inspired by the fact that isobaric surfaces coincide with the equipotential shells when stars are in the hydrostatic equilibrium. This makes the concepts of volume-effective radii and average effective acceleration of each shell a valuable tool to simulate binary stars in a 1D stellar evolution code.

Our method for obtaining the volume-equivalent radii of each equipotential shell is to integrate with spherical volume elements from the vicinity of the center of the donor star up to the point where the corresponding potential is equal to that sought, with fixed precision. The average effective acceleration on each shell is obtained by dividing each shell into triangular mesh areas and then calculating the weighted average of the effective acceleration, with the weight being the area of the triangular mesh element. The integration area includes L_1 -plane. In addition, we obtained the

effective accelerations averaged on the L_1 -plane as a function of the cross-sectional area or effective potential (the semi-major and semi-minor axes of these ellipse-like cross-sections are also tabulated). Values on the equipotential shell only (excluding L_1 -plane) can be recovered from the two provided values. We also obtained the average inverse effective acceleration, averaged over the entire equipotential level and on the L_1 -plane.

We provide the tables for a range of mass ratios, from 10^{-6} to 10^5 . We have verified the provided tables for self-convergence by taking the run for several angular resolutions. We have also validated the tables by comparing our results to the fit provided for the volume equivalent radius of the shell passing through L_1 by [19], the fit provided for the volume equivalent radius of the shell passing through the outer Lagrange point by [31] and the average effective acceleration of shells passing through L_1 and L_2 tabulated by [18] for certain mass ratios.

Further, we provide analytical expressions describing the effective acceleration's behavior in the vicinity of the center of the donor star in order to check whether our numerical tables work well close to the center. We also describe a rapid method to obtain effective accelerations for the non-point mass profiles that can take place in stars, using our pre-calculated table for point-mass calculations. This rapid method has been tested and verified to agree with the results for integrating the polytropic mass distribution for $n = 1.5$ and $n = 3$, encompassing most of the mass distributions that are plausible in stars.

We have provided a subroutine for the community that can be used in any 1D stellar code to rapidly obtain effective accelerations (as a function of the local mass and radius) that are more appropriate for the case of binary stars. We hope that the method, the tables, and the subroutine will help with further progress in the understanding of binary star evolution.

N.I. acknowledges funding from NSERC Discovery under Grant No. NSERC RGPIN-2019-04277. This research was enabled in part by support provided by Com-

pute Canada (www.computecanada.ca).

APPENDIX

A. DESCRIPTION OF THE TABLES

We provide one file for each of the 109 calculated mass ratios q between 10^{-6} and 10^5 . The file’s name contains the value of $\log_{10} q$ for which it was obtained. Each file has 15 columns of data, as described in Table 2.1. There are 600 data points (rows) for each table, starting from $\xi = \xi(0.05x_{L_1}, 0, 0)$ to $\xi = \xi_{\text{Louter}}$. The equipotential shell passing via L_1 is the data point number 500.

Columns 3–8 of data provide values at the equipotential shells at all data points as obtained from 3D integrations. Hence, the equipotential shells are inclusive of the L_1 -plane; the truncated equipotential areas and values on them are to be reconstructed as described in § 2.4.7. The columns 9–14 provide data for the L_1 -plane but only for mass ratios $\log_{10} q \leq 2.5$ (a regime where stellar interactions may lead to a mass transfer with a non-negligible mass stream thickness). The L_1 -plane properties are given only at the rows 501–600 for the equipotentials less to the L_1 value. In rows 1–500, columns 9–14 are filled with the “0” value as a placeholder. For $\log_{10} q > 2.5$, columns 9–14 for rows 501–600 are filled with the “0” value. For point mass cases, one needs three quantities, the donor star mass M_1 , the mass ratio q , and the binary separation a , to recover values in CGS. The conversions can be found in Table 2.1.

Another set of files we provide on the website includes a compact version of the previously mentioned. In this version, the units of potential and effective acceleration have been provided in terms of a single point-mass star’s potential and acceleration, respectively. This version of the table and the relevant conversion units are tabulated in Table 2.2. This table is used by the code described in Appendix 2.6 to obtain effective accelerations.

Table 2.1: The properties computed and included in our database for each mass ratio.

	quantity	notation	conversion equation
1	equipotential shell number		
2	mass ratio	q	unitless
3	fill-out function	F	unitless
4	potential	ξ	$\xi \times \frac{-GM_1(1+q)}{2qa}$
5	volume-equivalent radius	R_{eq}	$R_{\text{eq}} \times a$
6	effective acceleration averaged on the equipotential shell	η_{shell}	$\eta_{\text{shell}} \times \frac{GM_1(1+q)}{2qa^2}$
7	inverse effective acceleration averaged on the equipotential shell	$\langle \eta_{\text{shell}}^{-1} \rangle$	$\langle \eta_{\text{shell}}^{-1} \rangle \times \frac{2qa^2}{GM_1(1+q)}$
8	area of the equipotential shell	A	$A \times a^2$
9	area of L_1 cross-section	A_{Lpl}	$A_{\text{Lpl}} \times a^2$
10	y intersection of L_1 cross-section	y_{Lpl}	$y_{\text{Lpl}} \times a$
11	z intersection of L_1 cross-section	z_{Lpl}	$z_{\text{Lpl}} \times a$
12	effective acceleration averaged over the intersection with L_1 -plane	η_{L}	$\eta_{\text{L}} \times \frac{GM_1(1+q)}{2qa^2}$
13	effective acceleration averaged over L_1 cross-section area	η_{Lpl}	$\eta_{\text{Lpl}} \times \frac{GM_1(1+q)}{2qa^2}$
14	inverse effective acceleration averaged over L_1 cross-section area	$\langle \eta_{\text{Lpl}}^{-1} \rangle$	$\langle \eta_{\text{Lpl}}^{-1} \rangle \times \frac{2qa^2}{GM_1(1+q)}$

In addition, a file has been provided with properties corresponding to the first three Lagrange points for all mass ratios computed, see Table 2.3. For mass ratios lower than 1, where the outer Lagrange point is L_2 , and L_3 is on the opposite side, we have filled -1 for properties corresponding to L_3 ; the same has been applied for columns 5 and 6 of mass ratios with $\log_{10} q > 2.5$.

There are two more supplementary tables (see §2.4.7). One of them is very similar to Table 2.1, but 3D quantities were obtained while doing integrations over truncated equipotentials. The second supplementary table provides values of η_x integrated on L_1 -plane.

B. Subroutine for Effective Acceleration

The subroutine that we provide uses as input M_1 , r_1 (distance from the center of the donor star), $M_{1,\text{loc}}$ (enclosed mass of the star from the center up to r_1), M_2 , and a . By choice of the user, it returns either value of the effective acceleration in CGS, or

Table 2.2: The compact version of the database that will be used in B

	quantity	notation	conversion equation
1	volume-equivalent radius	R_{eq}	$R_{\text{eq}} \times a$
2	relative potential	ξ_{rel}	$\xi_{\text{rel}} \times \frac{-GM_1}{r_{\text{eq}}}$
3	relative average effective acceleration on equipotential shell	$\eta_{\text{rel,shell}}$	$\eta_{\text{rel,shell}} \times \frac{GM_1}{r_{\text{eq}}^2}$
4	relative average effective acceleration on L_1 cross-section	$\eta_{\text{rel,Lpl}}$	$\eta_{\text{rel,Lpl}} \times \frac{GM_1}{r_{\text{eq}}^2}$
5	area of L_1 cross-section	A_{Lpl}	$A_{\text{Lpl}} \times a^2$
6	area of equipotential shell	A	$A \times a^2$

Table 2.3: The properties computed and included in our database for each of the first three Lagrange points.

quantity	notation	conversion equation
1	mass ratio	q unitless
2	volume-equivalent radius of shell passing L_1	$R_{\text{eq,L1}}$ $R_{\text{eq,L1}} \times a$
3	volume-equivalent radius of shell passing L_2	$R_{\text{eq,L2}}$ $R_{\text{eq,L2}} \times a$
4	volume-equivalent radius of shell passing L_3	$R_{\text{eq,L3}}$ $R_{\text{eq,L3}} \times a$
5	area of L_1 cross-section of L_2 shell	$A_{\text{Lpl,L2}}$ $A_{\text{Lpl,L2}} \times a^2$
6	area of L_1 cross-section of L_3 shell	$A_{\text{Lpl,L3}}$ $A_{\text{Lpl,L3}} \times a^2$
7	average effective acceleration on the Lplane of L_2 shell	$\eta_{\text{Lpl,L2}}$ $\eta_{\text{Lpl,L2}} \times \frac{GM_1(1+q)}{2qa^2}$
8	average effective acceleration on the Lplane of L_3 shell	$\eta_{\text{Lpl,L3}}$ $\eta_{\text{Lpl,L3}} \times \frac{GM_1(1+q)}{2qa^2}$

the effective acceleration as a fraction of the single star’s effective acceleration. The values are for the truncated equipotentials. Our subroutine that uses these databases gives the effective acceleration as a function of the masses of the two stars, the orbital separation, and the distance from the center of the donor star. Once the mentioned inputs to the subroutine are given, the code determines between which two mass ratios does the local mass ratio fall in between. Then for those two tables it finds where the distance from the donor star’s center falls in between and interpolates for the effective acceleration between the two volume equivalent radii. After doing this for both mass ratios, it interpolates again, this time between mass ratios and the two obtained accelerations corresponding to those mass ratios to obtain the finalized effective acceleration. This acceleration could be given in CGS units, or as a unitless parameter by dividing it by the local gravitational acceleration if there was only a single star.

If the mass ratio specified is lower than the minimum mass ratio in the database (10^{-6}), or larger than the maximum mass ratio (10^{+5}), the code will output an error. If the distance and orbital separation is specified such that $r_1/a \leq 0.05$, the subroutine will use the analytical expression 2.40 to obtain the effective acceleration instead. The code as it is should not be used for the cases when the mass ratio is above $10^{+2.5}$, and there is RLOF. In the latter case, the user should re-do this table using 3D quantities obtained while doing integrations over truncated equipotentials. The databases and sample subroutines are available at Zenodo [35], and updates will be available at https://github.com/AliPourmand/1D_binary_star_properties.

C. Behavior Close to the Center of M_1

We consider a coordinate system in corotation with the binary, with the origin at the donor star’s center. The xy plane is the plane of the orbit, and the co-rotating plane is rotating around the axis which passes through the center of mass of the binary system. The effective potential Ψ in a spherical coordinate system that rotates with

the fixed binary orbital angular velocity $\Omega = \sqrt{G(M_1 + M_2)/a^3}$:

$$\begin{aligned} \Psi(R, \vartheta, \varphi) = & -\frac{GM_1}{R} - \frac{GM_2}{\sqrt{(R \cos \varphi \sin \vartheta - a)^2 + R^2 \sin^2 \varphi \sin^2 \vartheta + R^2 \cos^2 \vartheta}} \\ & - \frac{1}{2} \Omega^2 \left[\left(R \cos \varphi \sin \vartheta - a \frac{M_2}{M_1 + M_2} \right)^2 + R^2 \sin^2 \varphi \sin^2 \vartheta \right]. \end{aligned} \quad (2.34)$$

Here M_1 and M_2 are the donor and companion star masses, a is the orbital separation, and R is the distance to the origin.

The first term Ψ_{ss} is the potential of a spherically symmetric single star of mass M_1 . The other two terms represent the deviation of the effective potential $\Delta\Psi = \Psi_{\text{c}} + \Psi_{\text{b}}$ due to having a companion of mass M_2 , Ψ_{c} , and due to being in a coordinate system that rotates with Ω , Ψ_{b} . Introducing $r = R/a$, the terms are reduced to:

$$\begin{aligned} \Psi_{\text{ss}}(r, \vartheta, \varphi) &= -\frac{GM_1}{a} \frac{1}{r}, \\ \Psi_{\text{c}}(r, \vartheta, \varphi) &= -\frac{GM_2}{a} \frac{1}{\sqrt{r^2 - 2r \cos \varphi \sin \vartheta + 1}}, \\ \Psi_{\text{b}}(r, \vartheta, \varphi) &= -\frac{1}{2} \frac{G(M_1 + M_2)}{a} \left[r^2 \sin^2 \vartheta \right. \\ &\quad \left. - 2r \frac{M_2}{M_1 + M_2} \cos \varphi \sin \vartheta + \frac{M_2^2}{(M_1 + M_2)^2} \right]. \end{aligned} \quad (2.35)$$

We want to investigate the behavior of the effective acceleration and potential at distances close to the center; thus we assume that equipotential surfaces there are almost spherical (we have verified this assumption by numerical integrations).

C.1. *Effective acceleration*

As the equipotential surfaces are almost spherical, we adopt that for the effective acceleration, the only derivative of the effective potential that matters is the derivative by r .

$$\begin{aligned} \frac{\partial \Delta \Psi(r, \vartheta, \varphi)}{\partial r} &= \frac{G}{a} [M_2 \frac{(r - \cos \varphi \sin \vartheta)}{(r^2 - 2r \cos \varphi \sin \vartheta + 1)^{3/2}} \\ &- (M_1 + M_2)r \sin^2 \vartheta + M_2 \cos \varphi \sin \vartheta] . \end{aligned} \quad (2.36)$$

In the limit $r \ll L_1$,

$$\left. \frac{\partial \Delta \Psi(r, \vartheta, \varphi)}{\partial r} \right|_{r \ll 1} = \frac{G}{a} [M_2(r - 3r \cos^2 \varphi \sin^2 \vartheta) - (M_1 + M_2)r \sin^2 \vartheta] . \quad (2.37)$$

After the integration over all angles, the only contributing term that remains is from being in the co-rotating frame, while the contribution of the gravitational field of the companion has vanished:

$$\begin{aligned} &\left\langle \left. \frac{\partial \Delta \Psi(r, \vartheta, \varphi)}{\partial r} \right|_{r \ll 1} \right\rangle \\ &= \frac{1}{4\pi} \int_{4\pi} \left. \frac{\partial \Delta \Psi(r, \vartheta, \varphi)}{\partial r} \right|_{r \ll 1} d\Omega = -\frac{2}{3} \frac{G(M_1 + M_2)}{a} r . \end{aligned} \quad (2.38)$$

Finally, the relative deviation of the gradient of the effective potential in a binary, from the case of the spherically symmetric one, near the center, is

$$\begin{aligned} &\left\langle \left. \frac{\partial \Delta \Psi(r, \vartheta, \varphi)}{\partial r} \right|_{r \ll 1} \right\rangle / \frac{\partial \Psi_{ss}(r)}{\partial r} = -\frac{2}{3} \frac{(M_1 + M_2)}{M_1} r^3 \\ &= -\frac{2}{3} \frac{(M_1 + M_2)}{M_1} \frac{R^3}{a^3} . \end{aligned} \quad (2.39)$$

Converting to the unitless acceleration used throughout in this manuscript, and realising that r used in here is equivalent to r_1 , we have for the deviation in the average effective acceleration due to being in a binary:

$$\Delta \eta = -\frac{2}{3} \frac{1+q}{q} r_1^3 \eta_{ss} . \quad (2.40)$$

Here η_{ss} is the the average effective acceleration of a spherically symmetric single star, and $q = M_1/M_2$.

C.2. Potential

In the limit $r \ll 1$, the second term that provides the effect due to having a companion is:

$$\Psi_c(r, \vartheta, \varphi) = -\frac{GM_2}{a} \left(1 + r \cos \varphi \sin \vartheta - \frac{r^2}{2} \right). \quad (2.41)$$

After the integration over all angles, we have:

$$\langle \Delta \Psi(r, \vartheta, \varphi) |_{r \ll 1} \rangle / \Psi_{ss}(r) = \frac{3M_2^2 + 2M_1M_2}{2M_1(M_1 + M_2)} r + \frac{2M_1 + 5M_2}{6M_1} r^3, \quad (2.42)$$

and, for the unitless potential, with $q = M_1/M_2$:

$$\Delta \xi = \left(\frac{3 + 2q}{2q(1 + q)} r_1 + \frac{2q + 5}{6q} r_1^3 \right) \xi_{ss}. \quad (2.43)$$

C.3. Effective acceleration for non-point mass

The derivation for non-point mass is similar to described in C.1, with the difference that in the Equation 2.34, the total mass M_1 in the first term (Ψ_{ss}) is replaced by the local value of mass,

$$\Psi_{ss,loc}(r, \vartheta, \varphi) = -\frac{GM_{loc}}{a} \frac{1}{r}. \quad (2.44)$$

Here M_{loc} is the local mass coordinate inside the donor star at a distance r from the star's center. Thus, the effective acceleration of a single, non-point mass star at radius r and with local mass M_{loc} is:

$$\frac{\partial \Psi_{ss,loc}(r)}{\partial r} = \frac{GM_{loc}}{a} \frac{1}{r^2}. \quad (2.45)$$

$$\begin{aligned}
& \left\langle \frac{\partial \Delta \Psi(r, \vartheta, \varphi)}{\partial r} \Big|_{r \ll 1} \right\rangle / \frac{\partial \Psi_{\text{ss,loc}}(r)}{\partial r} \\
&= -\frac{2(M_1 + M_2)}{3 M_{\text{loc}}} r^3 \equiv -\frac{2(M_1 + M_2) R^3}{3 M_{\text{loc}} a^3}. \tag{2.46}
\end{aligned}$$

The unitless form of the following equation could be obtained if we use the fact that the scaling factor for effective acceleration 2.12 is the same for both terms of the numerator and the denominator of the left-hand side, we can write the left hand side as:

$$\left\langle \frac{\partial \Delta \Psi(r, \vartheta, \varphi)}{\partial r} \Big|_{r \ll 1} \right\rangle / \frac{\partial \Psi_{\text{ss,loc}}(r)}{\partial r} = \frac{\Delta \eta_{\text{loc}}}{\eta_{\text{ss,loc}}} \tag{2.47}$$

And, finally, using the definition of q_{loc} :

$$\Delta \eta_{\text{loc}} = -\frac{2}{3} \frac{1+q}{q_{\text{loc}}(r_1)} r_1^3 \eta_{\text{ss,loc}}. \tag{2.48}$$

Chapter 3

Application: Initial conditions of Common Envelope Events

3.1 Introduction

This thesis aims to investigate the initial conditions of the CE phase. In this chapter, we have first discussed in § 3.2 how we couple our subroutine with the stellar evolution code `MESA` to include the effective acceleration of binary systems. In § 3.3 we have described the initial parameters of the grid of binary systems we have simulated. In § 3.4 we describe the three methods we use to carry out these simulations.

Then, in §3.5, we present and discuss the results of the grid, by comparing the results obtained by each method. §3.6 is then focused on a scenario in which the difference between these three methods is extreme. Finally, in §3.7, we discuss the result of simulating V1309 Scorpii’s progenitor up to the donor star’s RLOF.

3.2 Modifying gravitational field in MESA

To explore the effect of the modified gravitational field on a star that evolves in a binary system, we will use the stellar evolution code `MESA`. `MESA` uses the following equation in each mesh zone to calculate the gravitational acceleration g_{MESA}

$$g_{\text{MESA}} = c_{\text{grav}}(R_{\text{loc}}) \frac{M_{\text{loc}}}{R_{\text{loc}}^2}. \quad (3.1)$$

Here `cgrav` is a variable defined in `MESA`. By default, it equals the value of Newton’s gravitational constant G . However, since it is a variable, it can be considered a function of the mesh zone’s local mass M_{loc} and radius R_{loc} coordinates, and hence it can be altered for each mesh zone.

We implement the subroutine described in Appendix 2.6 into `MESA` to obtain the effective acceleration¹. This subroutine allows us to find the binary g_{eff} for any mesh point inside the considered star. g_{eff} is a function of the mesh point’s local mass and radius coordinates, as well as the total mass of each star and the orbital separation.

The subroutine can return g_{eff} either in CGS or as a fraction of what an isolated single star would feel at that mass and radius coordinate – in other words, it provides $g_{\text{eff}}/g_{\text{MESA}}$. The convenient way to alter `cgrav` is using the latter form, which we do so with the following equation

$$\text{cgrav}_{\text{eff}}(R_{\text{loc}}, q_{\text{loc}}, q_{\text{tot}}, a) = \frac{g_{\text{eff}}}{g_{\text{MESA}}} \times \text{cgrav}(R_{\text{loc}}). \quad (3.2)$$

Then the effectively acting acceleration that all stellar structure equations are evolved within `MESA`’s is

$$g_{\text{eff}} = \text{cgrav}_{\text{eff}}(R_{\text{loc}}, q_{\text{loc}}, q_{\text{tot}}, a) \frac{M_{\text{loc}}}{R_{\text{loc}}^2}. \quad (3.3)$$

Thus, by incorporating the subroutine in `run_star_extras` (a file that enables users to modify how `MESA` works), we can successfully change the effective acceleration throughout the donor star at each timestep of evolution.

3.3 Grid of Simulations

We select 4 initial masses for the donor star, $M_1 = 1, 3, 7$ and $15M_{\odot}$, 4 mass ratios for the binary system, $q = 0.5, 1, 2$ and 10 , and 7 final radii to evolve the donor star to, as the grid of simulations, $2, 5, 20, 50, 100, 200$ and 500 , see Table 3.1. This grid

¹This is possible via the `use_other_cgrav` option in `MESA`

Table 3.1: Table including the mass ratios q (first row), final radii r_f (first column), and orbital separations (in solar radii) of our grid of initial conditions (the terms in parenthesis indicate the value of orbital separation for $M_1 = 3M_\odot$ stars which as explained, we have set their evolution to end at $45R_\odot$ instead of $50R_\odot$. Note that these selections will be used for each initial donor mass specified.

$r_f \backslash q$	0.5	1	2	10
$2R_\odot$	6.23	5.27	4.54	3.45
$5R_\odot$	15.58	13.19	11.36	8.64
$20R_\odot$	62.34	52.78	45.45	34.54
$50R_\odot$ ($45R_\odot$ for $M_1 = 3M_\odot$)	155.86 (140.28)	131.95 (118.76)	113.63 (102.27)	86.47 (77.83)
$100R_\odot$	311.73	263.9	227.27	172.95
$200R_\odot$	623.46	527.81	454.54	345.91
$500R_\odot$	1558.66	1319.53	1136.35	864.79

of $4 \times 4 \times 7$ setups allows us to explore the parameter space of initial conditions for the CE phase. There is an exception. $3M_\odot$ star, at about $r_f = 50R_\odot$, is changing its evolutionary stage from Hydrogen shell burning to He core burning. As a result, a slight change in the radius at RLOF could lead to selecting a stellar model either before or after He core burning, and the models will have naturally vastly different structures. For the $3M_\odot$ star, we use $r_f = 45R_\odot$.

3.4 Three Approaches

To evaluate the effect of “true” effective acceleration, we will model the evolution of each case in our grid using three different approaches:

1. **modified gravity** – MESA for single star evolution coupled with our modified gravitational acceleration subroutine for binary systems.
2. **standard** MESA’s standard binary package.
3. **fully synchronized** MESA’s standard binary package, including tidal evolution and orbital synchronization.

We consider that Cases 2 and 3 are the two limiting cases, as they represent no rotation and the maximum allowed rotation. Our modified gravity, Case 1, is expected to be close to Case 3, though see §2.4.5, where we showed that the effective acceleration in a binary could differ from a solid rotation case up to 20 percent.

First, we choose the values at which we want the donor stars to fill their Roche lobes. We use then Eggleton’s relation [19] to find the orbital separation when the star is at the RLOF

$$a = \frac{0.6q^{2/3} + \ln(1 + q^{1/3})}{0.49q^{2/3}} R_{L1} . \quad (3.4)$$

The input for the simulations is the initial orbital separation a . A sample inlist for each of the 3 methods for one of the cases in our grids is provided in Appendix B.

It is important to note that the goal of our study is not to perform proper binary evolution but to disentangle and evaluate the effect of taking into account binary physics on the stellar structure. We hence keep a star in a binary with a fixed orbital separation. At the same time, the donor star is held in the state of corotation with the binary in the first and third approaches. Therefore, in our simulations, there is no orbital angular momentum loss or transfer, and the system’s total angular momentum (including the angular momentum of the donor) doesn’t change. Conserving the total angular momentum while allowing the angular momentum transfer from the orbit to the donor would lead to vastly different evolutionary paths to RLOF. It would make the task of pinpointing the effect of using the different binary physics almost impossible.

3.5 Results of the Grid Runs

We use the locations on the HR diagram where the donor stars overflow their Roche Lobes as the primary diagnostic to monitor the difference between the three methods. Figures 3.1-3.4 show the results for four mass ratios. The evolutionary track of

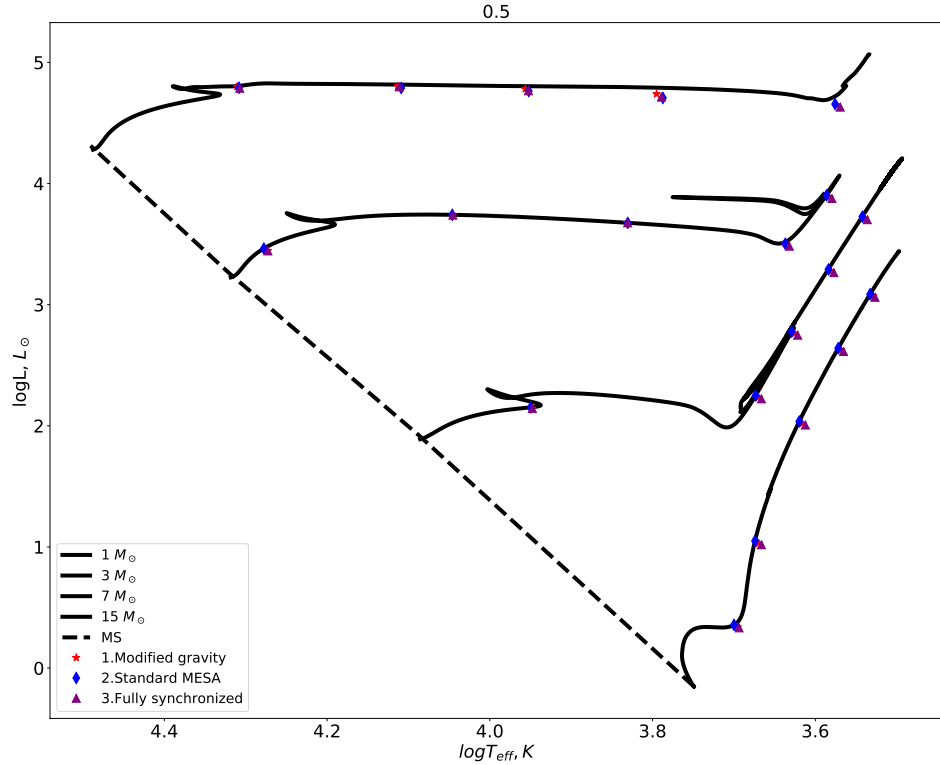


Figure 3.1: Position on the HR diagram of the simulations with $q = 0.5$ when the donor star has reached Roche Lobe Size. The red star indicates the final point using method 1, the blue diamond indicates method 2, and the purple triangle indicates the result using method 3 (the three methods were explained in 3.4). The solid black lines depict the evolutionary tracks of single stars with the same initial conditions the donor star has. The black dashed line is the MS branch.

simulation with various binary physics follow each other closely, and there isn't much use in showing their entire evolutionary tracks.

The endpoints for most of the simulations were obtained with a relative tolerance of 0.1%, or, in other words, the final stellar model's radius was obtained within 0.1% of the requested r_f . The exception is the set of simulations with $M_1 = 15M_{\odot}$ and $r_f = 500R_{\odot}$, where the best relative tolerance we could achieve is 1%.

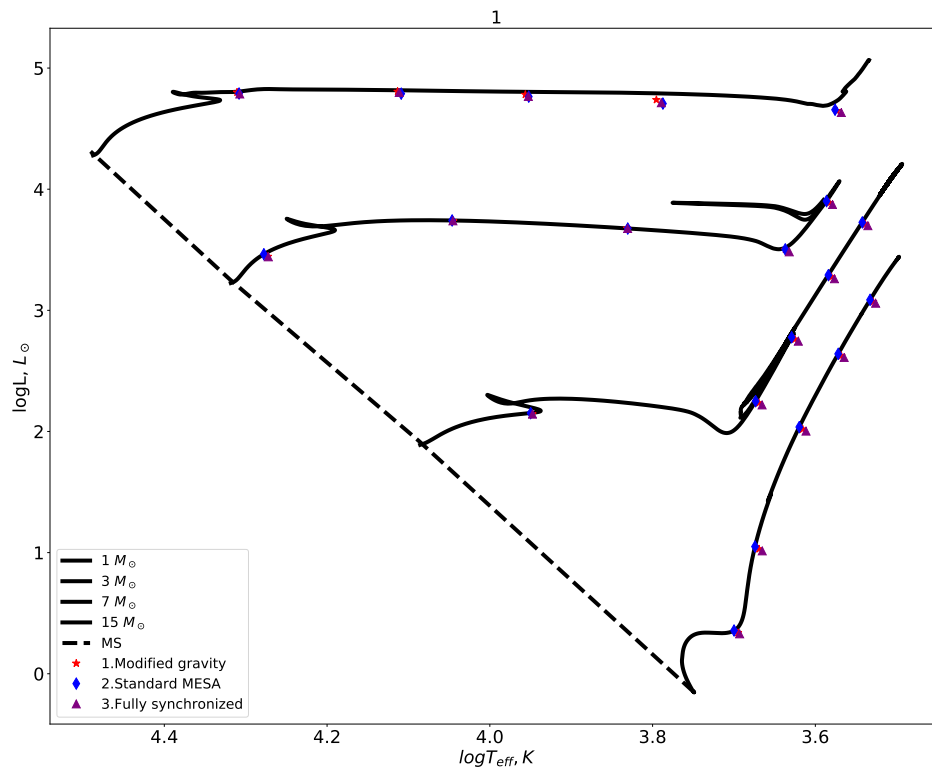


Figure 3.2: Figure similar to figure 3.2, for mass ratios $q = 1$.

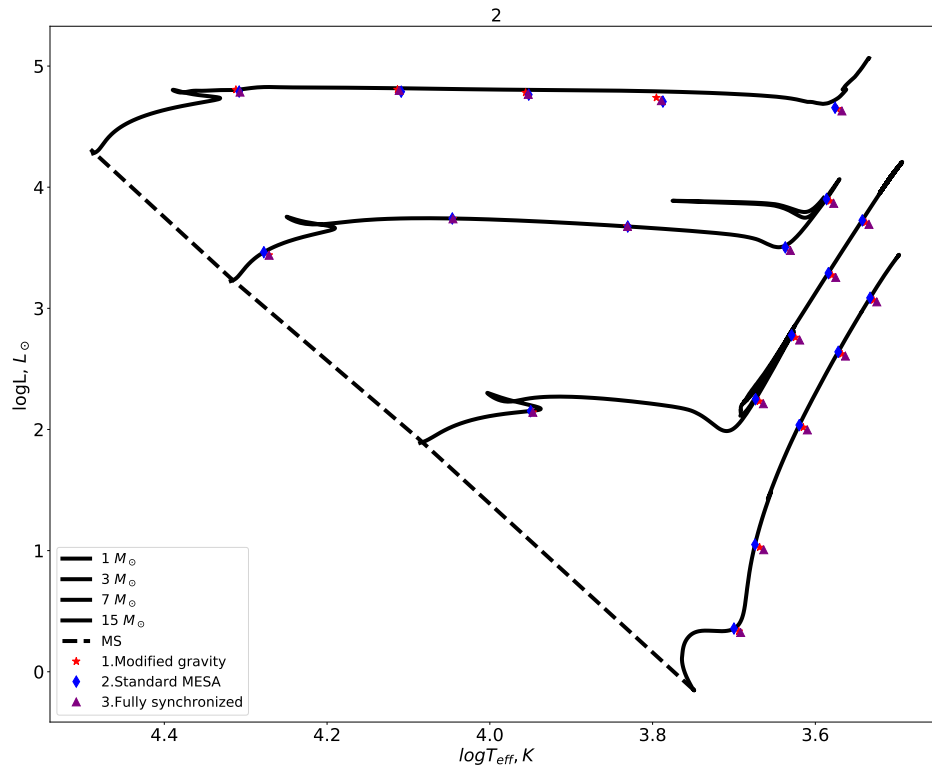


Figure 3.3: Figure similar to figure 3.2, for mass ratios $q = 2$.

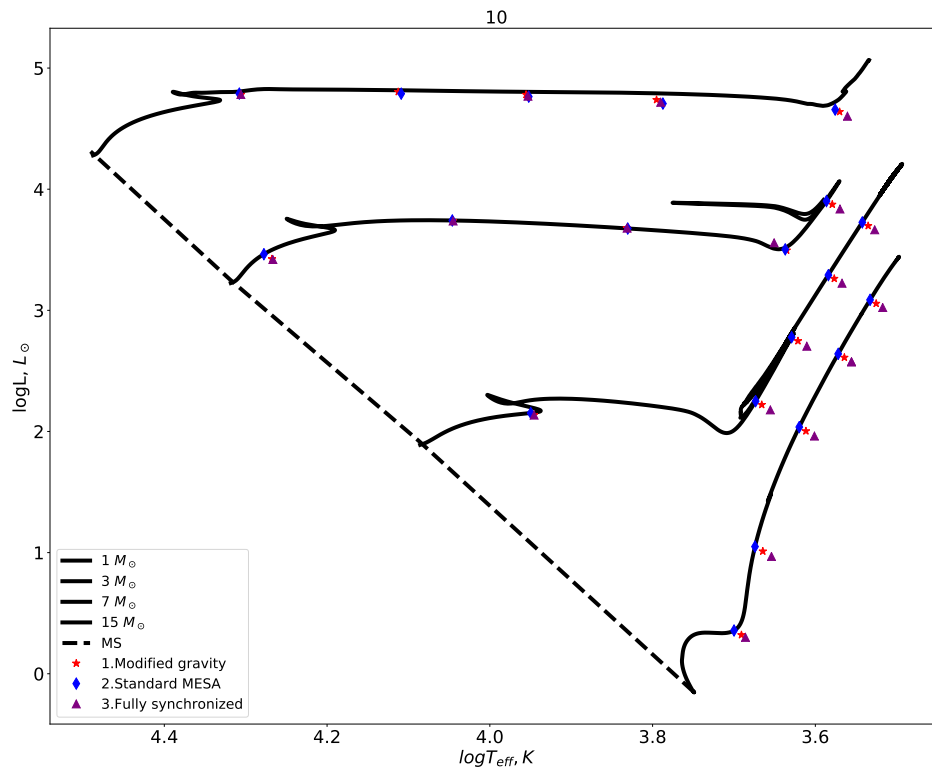


Figure 3.4: Figure similar to figure 3.2, for mass ratios $q = 10$.

3.5.1 Discussion

Several implications could be made from these figures, which are listed below:

1. Overall, it could be said that the difference in the final point on the HR diagram is relatively small
2. With increasing mass ratio, the spaces between the three methods' final points mostly seem to increase
3. It could also be inferred that for greater final radii (meaning more evolved stars), the deviation between the 3 methods seems to increase
4. We notice that most final positions obtained with method 1 fall between method 2 and method 3, as expected.

3.6 Initial Conditions Resulting in Extreme Deviations

As discussed in the previous section, the final position on the HR diagram, in most cases, doesn't vary significantly between methods 1-3. Although this is an outcome that one could expect from most initial parameters, there are some initial parameters where the difference between these methods could be extremely pronounced. This section discusses the outcome of simulating one such system to the Roche Lobe size. The initial conditions for this system are $M_1 = 3M_\odot$, $q = 10$, and $a = 22.14R_\odot$ (which gives $r_f = 12.8R_\odot$).

The evolutionary tracks that are obtained when simulating this system with the three methods are presented in Figure 3.5. As can be seen, the final position on the HR diagram that method 2 predicts is exceptionally far from the positions methods 1 and 3 predict.

To further investigate this simulation, we have plotted the adiabatic and radiative exponents of the donor star at the RLOF as the function of the radial coordinate

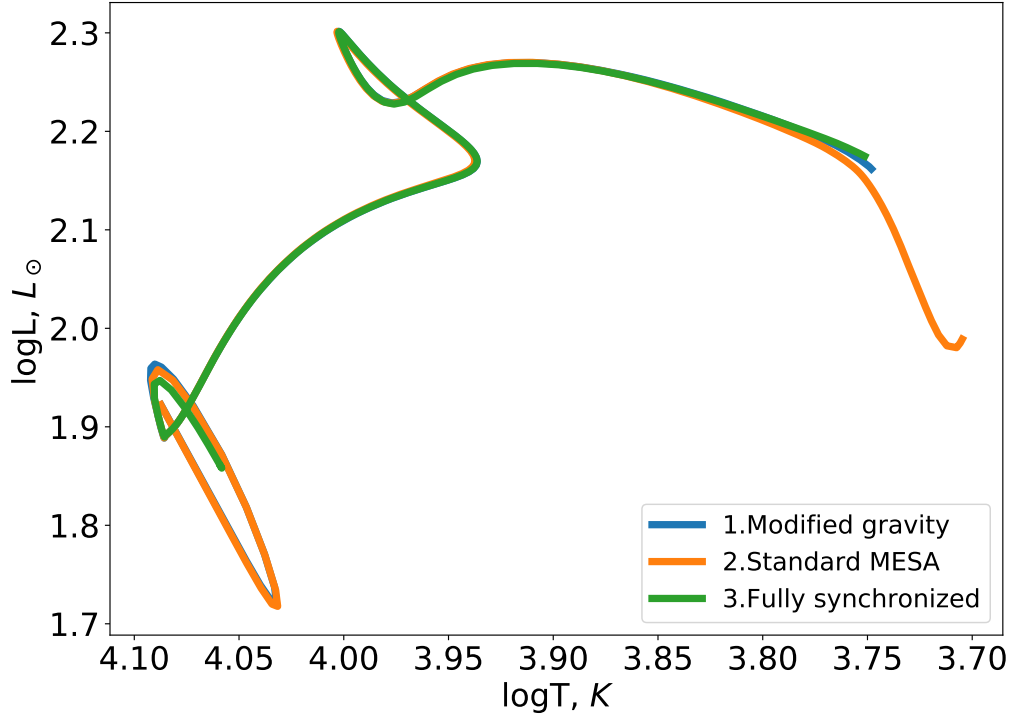


Figure 3.5: HR diagram showing evolutionary tracks for the donor star in the binary system described in Section 3.6 ($M_1 = 3M_\odot$, $q = 10$, and $a = 22.14R_\odot$), evolved up to the Roche Lobe size. The evolutionary tracks were obtained with the three methods described in Section 3.4.

for all three methods. The three methods all predict the donor star has developed a convective envelope at the onset of RLOF. However, the depth of the envelope varies for all three methods. Method 1 predicts the convective envelope stops at about $11R_\odot$, while for methods 2 and 3 this value changes to $7R_\odot$ and $12R_\odot$, respectively. The mass coordinate for where the convective envelope stops is about $2.54M_\odot$ for method 2. Meanwhile, methods 1 and 3 predict the outer convective envelope is only above the mass coordinate about $2.97M_\odot$.

The Kippenhahn diagram² for the evolution of this system with method 2 is shown in 3.7. As is apparent from this diagram, this external convective envelope that can

²the Kippenhahn diagram depicts the evolution of the internal structure of a star as a function of time

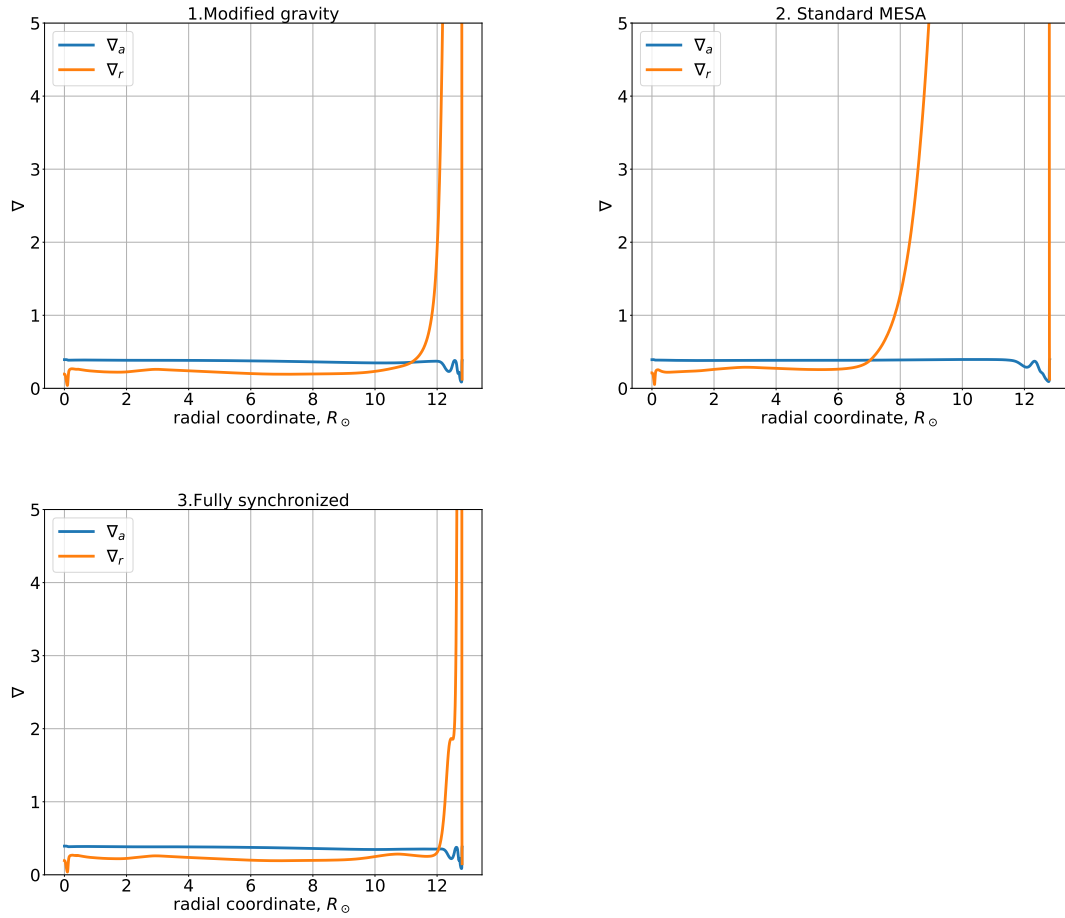


Figure 3.6: The adiabatic and radiative exponents that the 3 methods predict once the donor star described in Section 3.6 reaches the Roche Lobe size. Adiabatic exponents ∇_a are shown by the blue line, and Radiative exponents ∇_r are depicted with the orange line.

be seen in Figure 3.6 has just started developing at the end of the simulation.

This analysis reveals another interesting outcome: even though methods 1 and 3 predict relatively close locations on the HR diagram, the depth of the convective envelopes at that point are notably different from each other (in terms of radial coordinates). The depth of the convective envelope may play a decisive role in determining whether the possible mass transfer will be stable or unstable [37].

Hence, we make the two following conclusions:

1. Inclusion of the effects of effective binary acceleration could result in notable

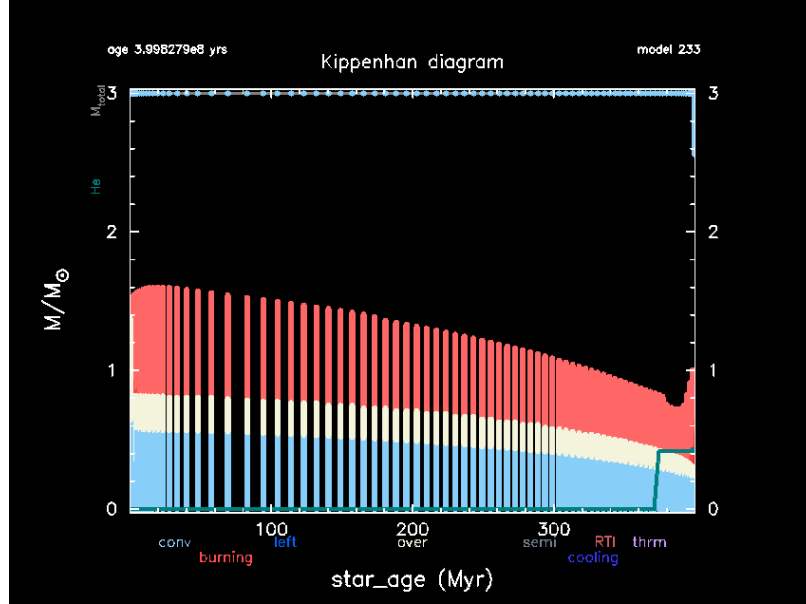


Figure 3.7: Kippenhahn diagram showing the evolution of internal structure of the donor star in the binary system described in Section 3.6 ($M_1 = 3M_\odot$, $q = 10$, and $a = 22.14R_\odot$). The horizontal axis shows the evolutionary time passed throughout the simulation in Mega years, and the vertical axis indicates the mass coordinate of the star. In a Kippenhahn diagram, different colors are used to differentiate between the physical processes happening in each mass coordinate. The abbreviations of these physical processes are written in color used to visualize them under the horizontal axis. The most notable physical processes in this star’s evolution are convective areas (light blue), nuclear burning (light red), and overshoot (cream). Towards the very end of the evolution, an external convective area has formed. This plot was created with MESA’s package for visualization `pgstar` [36].

differences between the simulation outcomes.

2. The proximity these three methods may predict on the HR diagram doesn’t necessarily entail similar internal structures.

3.7 Progenitor of the Observed Phenomena: V1309 Scorpii

We use the initial conditions mentioned for the progenitor in Section 1.5.1, which were $q = 10$, $M_1 = 1.52M_\odot$. We adopt the initial period as $P = 1.4$ days, as was observed before the outburst. We keep using the same assumption as for our grid

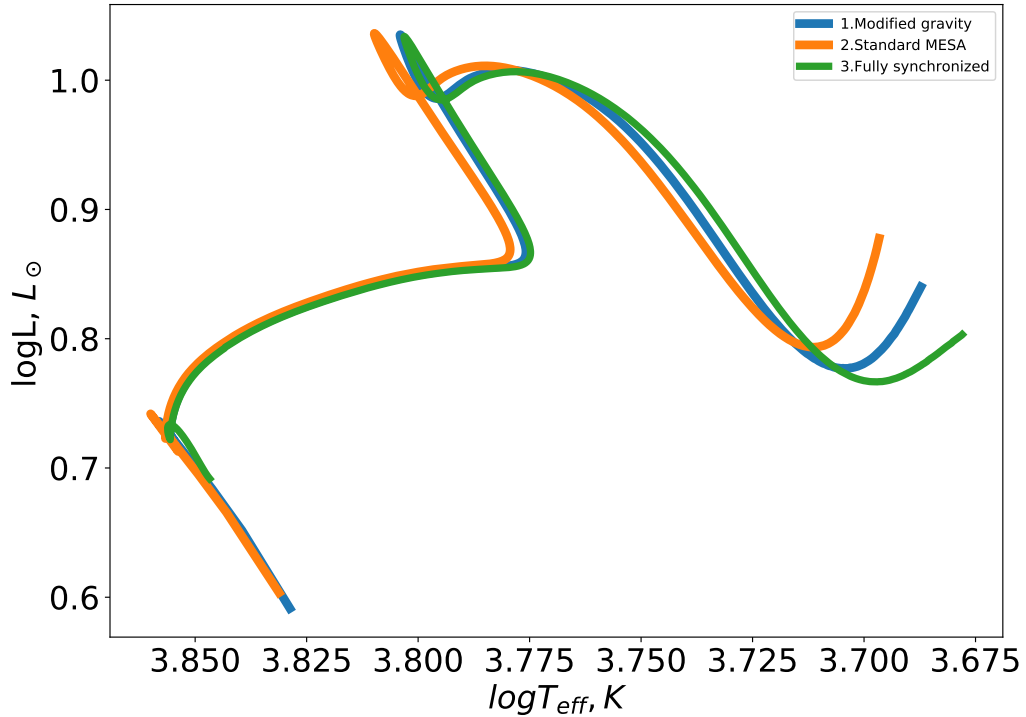


Figure 3.8: Evolutionary tracks of V1309 Sco.

of models that the orbital separation does not change throughout the evolution. We make use of an inlist that has been specifically designed to include the physics that is relevant in the case of V1309 Scorpii. This inlist has been previously used by [38] and can be seen in Appendix B, Listing B.5. The corresponding initial orbital separation is $a = 6.4R_{\odot}$, which provides the radius at the RLOF is $r_f = 3.7R_{\odot}$. We evolved this initial setup, using the three methods described in 3.4, up to the onset of the RLOF. The resulting evolutionary tracks can be seen in Figure 3.8. At the more advanced evolutionary stages (and larger radius), the evolutionary paths provided by the three methods get more distant from each other.

The effective temperature of the binary was measured to be about $T_{\text{eff}} \approx 4500K$ [26], with a $500K$ uncertainty [27]. Our simulations show that the donor star evolved with the modified gravity has $T_{\text{eff}} \approx 4870K$ at RLOF. This value is in the expected

range of values. However, we note that it does not significantly differ with methods 2 & 3, where the progenitor's effective temperature is found to be $\approx 4970K$ and $\approx 4760K$, respectively.

It should be stated that simulations performed using *MESA* can not account for the physical effects due to the contact between the two stars' surfaces. In a star that is strongly deformed due to proximity to its Roche lobe, the effective temperature is also not uniform and varies throughout the star's surface. Therefore, one should use 3D codes to properly model observable properties such as the effective temperature. For example, [38] has carried out 3D simulations for the progenitor of V1309 Scorpii using the *StarSmasher* code. Those simulations naturally obtained 3D surface distribution of the effective temperature of the donor star at the RLOF stage as a function of surface gravity.

Chapter 4

Summary and Ongoing Work

The primary goal of our thesis was to provide a method to include the effect of the gravitational fields of binary systems to use them in 1D stellar evolution codes. We also aimed to apply this method to simulate binary systems up to the RLOF. A summary of the main points in each chapter of the thesis is given in the following.

In Chapter 2, we have presented the database containing spacial and gravitational properties of the effective binary potential. The database was obtained for 109 mass ratios in the $[10^{-6}, 10^5]$ range. For each mass ratio, the database provides values for spatial coordinates from near the center of the donor star to the outer Lagrange point. We also provided an approximate method to utilize the database for simulating the effective acceleration of non-point mass donor stars as a function of the one-dimensional radial coordinate. We tested this method's accuracy by numerically integrating two different donor stars with polytropic mass distributions in a binary gravitational field, and comparing the values of the effective accelerations with what our approximate method finds. This method uses the analytical expression (Equation 2.40) we derived that calculates the donor star's effective acceleration in regions to the center of the donor star.

In Chapter 3, we first described how our method had been incorporated via a subroutine to `MESA` to simulate the evolution of binary stars with the effective gravity taken into account. We then described the grid of initial conditions for binary systems

we simulated up to the onset of the RLOF. The goal was to see how notable the effects of including the effective acceleration of binary stars could be. We also described two additional methods we use to evolve this grid. These two additional methods are used to compare our new approach with what MESA could traditionally predict for the evolution of these systems.

After plotting the results of this grid on the HR diagrams, we concluded that the final points of the evolutionary tracks on the (T_{eff}, L) plane – at the start of RLOF – of each of the three methods do not differ much from each other. However, we observed a growth in the separation between the final points obtained by the three methods as we increased the mass ratios q or the radii at the RLOF.

We also discussed the result of simulating a specific binary system where the outcome of one of the methods demonstrated a relatively significant difference in the final location on the HR diagram. After investigating the interior structure these three methods predict, we noticed that the depth of the convective envelope of the donor star obtained by each method notably differs from the other methods. We found out as a result of studying the internal structure of these simulations that proximity on the HR diagram doesn't necessarily imply similar internal structures.

In light of the mentioned simulations, we discovered that including the binary gravitational field causes the evolutionary tracks and the location on the HR diagram where the donor star fills its Roche Lobe to change from what is predicted by traditional approaches. The variation that this inclusion causes is a function of the mass ratio and the radius of the donor at the start of RLOF (which corresponds to the star's evolutionary stage at the exact moment). The final points on the HR diagram usually do not significantly differ from each other, although we discovered that exceptional cases do exist.

We also simulated an observed system that underwent a merger event: V1309 Scorpii. We simulated the progenitor donor star of V1309 Scorpii up to its RLOF with the three methods, and noticed some differences between the three predicted

evolutionary tracks. However, these differences were not that spectacular. Specifically for the case of the effective temperature T_{eff} at the final point of the simulation, the temperature that the three methods predicted all fell into the uncertainty range of the observed value.

We conclude this thesis by mentioning that the structure that the donor star has prior to the initiation of the MT is a more important question than the position on the HR diagram. More specifically, the energy budget of the expanded star is a key quantity in predicting the outcome of the CE phase (e.g., whether a merger event could happen or not). Calculating the binding energy from the outcomes of MESA simulations, which utilize our modified subroutine isn't a straightforward task. Thus, the remaining questions on this topic could be summarized in the following two points:

1. Devise a method to obtain the energy budget in a binary system before and after the CE event – similar to the standard energy formalism, but with the use of the novel 3D reduced approach we have developed
2. Calculate the energy budget in stellar models obtained using the three mentioned methods and then compare how much these values differ.

Bibliography

- [1] H. Sana *et al.*, “Binary Interaction Dominates the Evolution of Massive Stars,” *Science*, vol. 337, no. 6093, p. 444, Jul. 2012. DOI: 10.1126/science.1223344. arXiv: 1207.6397 [astro-ph.SR].
- [2] D. Raghavan *et al.*, “A Survey of Stellar Families: Multiplicity of Solar-type Stars,” *ApJS*, vol. 190, no. 1, pp. 1–42, Sep. 2010. DOI: 10.1088/0067-0049/190/1/1. arXiv: 1007.0414 [astro-ph.SR].
- [3] J. P. A. Clark and D. M. Eardley, “Evolution of close neutron star binaries,” *ApJ*, vol. 215, pp. 311–322, Jul. 1977. DOI: 10.1086/155360.
- [4] J. Abadie *et al.*, “Predictions for the rates of compact binary coalescences observable by ground-based gravitational-wave detectors,” *Classical and Quantum Gravity*, vol. 27, no. 17, p. 173001, Jul. 2010. DOI: 10.1088/0264-9381/27/17/173001.
- [5] M. Renzo *et al.*, “Prospects of gravitational wave detections from common envelope evolution with lisa,” *ApJ*, vol. 919, no. 2, p. 128, Oct. 2021. DOI: 10.3847/1538-4357/ac1110. [Online]. Available: <https://dx.doi.org/10.3847/1538-4357/ac1110>.
- [6] A. V. Tutukov and L. R. YungelSon, “The merger rate of neutron star and black hole binaries,” *MNRAS*, vol. 260, no. 3, pp. 675–678, Feb. 1993, ISSN: 0035-8711. DOI: 10.1093/mnras/260.3.675. eprint: <https://academic.oup.com/mnras/article-pdf/260/3/675/3837145/mnras260-0675.pdf>. [Online]. Available: <https://doi.org/10.1093/mnras/260.3.675>.
- [7] B. W. Carroll and D. A. Ostlie, *An Introduction to Modern Astrophysics*. 1996.
- [8] C. J. Hansen and S. D. Kawaler, *Stellar Interiors. Physical Principles, Structure, and Evolution*. 1994. DOI: 10.1007/978-1-4419-9110-2.
- [9] B. Paxton, L. Bildsten, A. Dotter, F. Herwig, P. Lesaffre, and F. Timmes, “Modules for Experiments in Stellar Astrophysics (MESA),” *ApJS*, vol. 192, no. 1, 3, p. 3, Jan. 2011. DOI: 10.1088/0067-0049/192/1/3. arXiv: 1009.1622 [astro-ph.SR].
- [10] B. Paxton *et al.*, “Modules for Experiments in Stellar Astrophysics (MESA): Planets, Oscillations, Rotation, and Massive Stars,” *ApJS*, vol. 208, no. 1, 4, p. 4, Sep. 2013. DOI: 10.1088/0067-0049/208/1/4. arXiv: 1301.0319 [astro-ph.SR].

- [11] B. Paxton *et al.*, “Modules for Experiments in Stellar Astrophysics (MESA): Binaries, Pulsations, and Explosions,” *ApJS*, vol. 220, 15, p. 15, Sep. 2015. DOI: 10.1088/0067-0049/220/1/15. arXiv: 1506.03146 [astro-ph.SR].
- [12] B. Paxton *et al.*, “Modules for Experiments in Stellar Astrophysics (MESA): Convective Boundaries, Element Diffusion, and Massive Star Explosions,” *ApJS*, vol. 234, no. 2, 34, p. 34, Feb. 2018. DOI: 10.3847/1538-4365/aaa5a8. arXiv: 1710.08424 [astro-ph.SR].
- [13] B. Paxton *et al.*, “Modules for Experiments in Stellar Astrophysics (MESA): Pulsating Variable Stars, Rotation, Convective Boundaries, and Energy Conservation,” *ApJS*, vol. 243, no. 1, 10, p. 10, Jul. 2019. DOI: 10.3847/1538-4365/ab2241. arXiv: 1903.01426 [astro-ph.SR].
- [14] A. S. Jermyn *et al.*, “Modules for Experiments in Stellar Astrophysics (MESA): Time-dependent Convection, Energy Conservation, Automatic Differentiation, and Infrastructure,” *ApJS*, vol. 265, no. 1, 15, p. 15, Mar. 2023. DOI: 10.3847/1538-4365/acaed8. arXiv: 2208.03651 [astro-ph.SR].
- [15] P. P. Eggleton, “The evolution of low mass stars,” *MNRAS*, vol. 151, p. 351, Jan. 1971. DOI: 10.1093/mnras/151.3.351.
- [16] P. Eggenberger *et al.*, “The Geneva stellar evolution code,” *Ap&SS*, vol. 316, no. 1-4, pp. 43–54, Aug. 2008. DOI: 10.1007/s10509-007-9511-y.
- [17] A. Weiss and H. Schlattl, “GARSTEC—the Garching Stellar Evolution Code. The direct descendant of the legendary Kippenhahn code,” *Ap&SS*, vol. 316, no. 1-4, pp. 99–106, Aug. 2008. DOI: 10.1007/s10509-007-9606-5.
- [18] S. Mochnacki, “Accurate integrations of the roche model,” *The Astrophysical Journal Supplement Series*, vol. 55, pp. 551–561, 1984.
- [19] P. P. Eggleton, “Approximations to the radii of roche lobes,” *ApJ*, vol. 268, p. 368, 1983.
- [20] G. Meynet and A. Maeder, “Stellar evolution with rotation. I. The computational method and the inhibiting effect of the μ -gradient,” *A&A*, vol. 321, pp. 465–476, May 1997.
- [21] J. P. Zahn, “Tidal friction in close binary systems.,” *A&A*, vol. 57, pp. 383–394, May 1977.
- [22] P. Hut, “Tidal evolution in close binary systems.,” *A&A*, vol. 99, pp. 126–140, Jun. 1981.
- [23] M. Livio and N. Soker, “The Common Envelope Phase in the Evolution of Binary Stars,” *ApJ*, vol. 329, p. 764, Jun. 1988. DOI: 10.1086/166419.
- [24] N. Ivanova, S. Justham, and P. Ricker, *Common Envelope Evolution*. 2020. DOI: 10.1088/2514-3433/abb6f0.
- [25] B. Paczynski, “Common Envelope Binaries,” in *Structure and Evolution of Close Binary Systems*, P. Eggleton, S. Mitton, and J. Whelan, Eds., vol. 73, Jan. 1976, p. 75.

- [26] R. Tylenda *et al.*, “V1309 scorpil: Merger of a contact binary,” *Astronomy & Astrophysics*, vol. 528, A114, Mar. 2011. DOI: 10.1051/0004-6361/201016221. [Online]. Available: <https://doi.org/10.1051/0004-6361/201016221>.
- [27] K. Stepień, “Evolution of the progenitor binary of V1309 Scorpil before merger,” *A&A*, vol. 531, A18, A18, Jul. 2011. DOI: 10.1051/0004-6361/201116689. arXiv: 1105.2627 [astro-ph.SR].
- [28] J. L. A. Nandez, N. Ivanova, and J. J. C. Lombardi, “V1309 sco—understanding a merger,” *ApJ*, vol. 786, no. 1, p. 39, Apr. 2014. DOI: 10.1088/0004-637X/786/1/39. [Online]. Available: <https://dx.doi.org/10.1088/0004-637X/786/1/39>.
- [29] K. Pavlovskii, N. Ivanova, K. Belczynski, and K. X. Van, “Stability of mass transfer from massive giants: double black hole binary formation and ultraluminous X-ray sources,” *MNRAS*, vol. 465, no. 2, pp. 2092–2100, Feb. 2017. DOI: 10.1093/mnras/stw2786. arXiv: 1606.04921 [astro-ph.HE].
- [30] Z. Kopal, *Close Binary Systems* (International astrophysics series). Wiley, 1959, ISBN: 9780471503255. [Online]. Available: <https://books.google.ca/books?id=cdk2AQAAIAAJ>.
- [31] P. Marchant *et al.*, “The role of mass transfer and common envelope evolution in the formation of merging binary black holes,” *Astronomy & Astrophysics*, vol. 650, A107, 2021.
- [32] R. Kippenhahn and H. C. Thomas, “A Simple Method for the Solution of the Stellar Structure Equations Including Rotation and Tidal Forces,” in *IAU Colloq. 4: Stellar Rotation*, A. Slettebak, Ed., Jan. 1970, p. 20.
- [33] A. S. Endal and S. Sofia, “The evolution of rotating stars. I. Method and exploratory calculations for a 7 M sun star,” *ApJ*, vol. 210, pp. 184–198, Nov. 1976. DOI: 10.1086/154817.
- [34] A. S. Endal and S. Sofia, “The evolution of rotating stars. II. Calculations with time-dependent redistribution of angular momentum for 7 and 10 M sun stars,” *ApJ*, vol. 220, pp. 279–290, Feb. 1978. DOI: 10.1086/155904.
- [35] A. Pourmand and N. Ivanova, *Properties of binary systems in a one-dimensional approximation*, 2023. DOI: 10.5281/zenodo.7576785. [Online]. Available: <https://zenodo.org/deposit/7576785>.
- [36] B. Paxton *et al.*, “Modules for Experiments in Stellar Astrophysics (MESA): Planets, Oscillations, Rotation, and Massive Stars,” *ApJS*, vol. 208, 4, p. 4, Sep. 2013. DOI: 10.1088/0067-0049/208/1/4. arXiv: 1301.0319 [astro-ph.SR].
- [37] K. Pavlovskii and N. Ivanova, “Mass transfer from giant donors,” *MNRAS*, vol. 449, no. 4, pp. 4415–4427, Jun. 2015. DOI: 10.1093/mnras/stv619. arXiv: 1410.5109 [astro-ph.SR].
- [38] R. W. M. Hatfull, N. Ivanova, and J. C. Lombardi, “Simulating a stellar contact binary merger – i. stellar models,” *Monthly Notices of the Royal Astronomical Society*, vol. 507, no. 1, pp. 385–397, Jul. 2021. DOI: 10.1093/mnras/stab2140.

Appendix A: Sample Inlists

Inlists are text files which give MESA commands on how to start, proceed with, and where to end the simulations.

Here, we have provided a sample inlist used for one of the stars evolved in figure 1.1.

```
1 &star_job
2   ! see star/defaults/star_job.defaults
3
4   ! begin with a pre-main sequence model
5   create_pre_main_sequence_model = .false.
6
7
8   ! display on-screen plots
9   pgstar_flag = .true.
10
11 / ! end of star_job namelist
12
13
14 &eos
15   ! eos options
16   ! see eos/defaults/eos.defaults
17
18 / ! end of eos namelist
19
20
21 &kap
22   ! kap options
23   ! see kap/defaults/kap.defaults
24   use_Type2_opacities = .true.
25   Zbase = 0.02
26
27 / ! end of kap namelist
28
29
30 &controls
31   ! see star/defaults/controls.defaults
32
33   ! starting specifications
34   initial_mass = 3 ! in Msun units
35   initial_z = 0.02
```

```
36
37
38
39 ! solver
40 ! options for energy conservation (see MESA V, Section 3)
41 energy_eqn_option = 'dedt'
42 use_gold_tolerances = .true.
43
44
45
46 / ! end of controls namelist
```

Listing A.1: sample inlist used to obtain 1.1

Appendix B: Sample Inlists for evolution up to RLOF

In this section, we have provided sample inlists that we will use to simulate the donor stars up to the Roche Lobe in Chapter 3, with the 3 different methods mentioned in Section 3.4. B.1 is the sample inlist used for method 1. B.2 is the sample inlist used for commanding the donor star’s evolution for methods 2 and 3. B.3 and B.4 are used for specifying the commands related to binary stellar evolution for methods 2 and 3 respectively.

The initial conditions such as donor star and companion star mass, initial orbital separation, and the photospheric radius’s upper limit will vary for the different initial conditions in the grid, but the rest of the commands stay the same. This is the case for all the simulations carried out in Chapter 3 with the exception of those related to V1309 Scorpii in Section 3.7. An inlist with more specific commands for the physics involved (such as stellar winds) was used in the case of V1309 Scorpii, whose inlist could be seen in B.5.

```
1 &star_job
2   ! see star/defaults/star_job.defaults
3
4   ! begin with a pre-main sequence model
5   create_pre_main_sequence_model = .false.
6
7   ! save a model at the end of the run
8   save_model_when_terminate = .true.
9   save_model_filename = 'last.mod'
10
11   write_profile_when_terminate=.true.
12   filename_for_profile_when_terminate='profile_last.data'
13   save_photo_when_terminate = .true.
14
```

```

15 ! display on-screen plots
16 pgstar_flag = .false.
17
18 change_initial_net = .true. ! switch nuclear reaction network
19 new_net_name = 'pp_and_cno_extras.net'
20 auto_extend_net = .true.
21 h_he_net = 'pp_and_cno_extras.net'
22 co_net = 'co_burn.net'
23 adv_net = 'approx21.net'
24
25
26 / ! end of star_job namelist
27
28
29 &eos
30 ! eos options
31 ! see eos/defaults/eos.defaults
32
33 / ! end of eos namelist
34
35
36 &kap
37 ! kap options
38 ! see kap/defaults/kap.defaults
39 use_Type2_opacities = .true.
40 Zbase = 0.02
41 kap_file_prefix = 'OP_gs98'
42 kap_lowT_prefix = 'lowT_fa05_gs98' ! for lower temperatures.
43
44
45 / ! end of kap namelist
46
47
48 &controls
49 ! see star/defaults/controls.defaults
50
51 ! starting specifications
52 initial_mass = 1 ! in Msun units
53 initial_z = 0.02
54 ! stop when photosphere_r is greater than this limit, in R_sun units
55 photosphere_r_upper_limit = 2
56
57 ! tolerance of stop
58
59 when_to_stop_atol = 0.d0
60 when_to_stop_rtol = 0.001d0
61
62 ! atmosphere
63 atm_option = 'T_tau'
64 atm_T_tau_relation = 'Eddington'
65 atm_T_tau_opacity = 'fixed'
66
67 ! options for energy conservation (see MESA V, Section 3)
68 max_abs_rel_run_E_err = -1

```

```

69  !!!!!!!!!!!!!!! option to use modified gravity subroutine
70
71
72      use_other_cgrav = .true.
73      ! for modified gravity
74
75  !!!!! inputs used in subroutines
76  !!mass ratio q= M1/M2
77      x_ctrl(1) = 0.5d0
78  !! orbital separation of the binary in solar radii
79      x_ctrl(2) = 6.23d0
80
81
82
83      mixing_length_alpha = 2.0
84      use_Ledoux_criterion = .false.
85
86
87      overshoot_scheme(1) = 'step'
88      overshoot_zone_type(1) = 'burn_H'
89      overshoot_zone_loc(1) = 'core'
90      overshoot_bdy_loc(1) = 'top'
91      overshoot_f(1) = 0.35
92      overshoot_f0(1) = 0.05
93
94
95  ! solver
96      ! options for energy conservation (see MESA V, Section 3)
97      energy_eqn_option = 'eps_grav'
98
99
100     use_gold_tolerances = .false.
101
102
103  ! output interval
104     terminal_interval = 1
105     history_interval = 1
106     profile_interval = 1
107     max_model_number = -1
108     max_num_profile_models = 10
109     photo_digits = 5
110     photo_interval = 50
111 / ! end of controls namelist

```

Listing B.1: sample inlist for method 1

```

1 &star_job
2   ! see star/defaults/star_job.defaults
3
4
5
6   ! begin with a pre-main sequence model
7   create_pre_main_sequence_model = .false.
8

```

```

9
10 ! save a model at the end of the run
11 save_model_when_terminate = .true.
12 save_model_filename = 'last.mod'
13
14
15
16 write_profile_when_terminate=.true.
17 filename_for_profile_when_terminate='profile_last.data'
18 new_rotation_flag = .true.
19 change_initial_rotation_flag = .true.
20 ! display on-screen plots
21 pgstar_flag = .false.
22
23
24
25 change_initial_net = .true. ! switch nuclear reaction network
26 new_net_name = 'pp_and_cno_extras.net'
27 auto_extend_net = .true.
28 h_he_net = 'pp_and_cno_extras.net'
29 co_net = 'co_burn.net'
30 adv_net = 'approx21.net'
31 save_photo_when_terminate = .true.
32
33
34
35 / ! end of star_job namelist
36
37
38 &eos
39 ! eos options
40 ! see eos/defaults/eos.defaults
41
42 / ! end of eos namelist
43
44
45 &kap
46 ! kap options
47 ! see kap/defaults/kap.defaults
48 use_Type2_opacities = .true.
49 Zbase = 0.02
50 kap_file_prefix = 'OP_gs98'
51 kap_lowT_prefix = 'lowT_fa05_gs98' ! for lower temperatures.
52
53
54 / ! end of kap namelist
55
56
57 &controls
58 ! see star/defaults/controls.defaults
59
60 ! stop when photosphere_r is greater than this limit, in R_sun units
61 photosphere_r_upper_limit = 2
62 initial_z = 0.02

```

```

63
64
65
66     ! tolerance of stop
67
68     when_to_stop_atol = 0.d0
69     when_to_stop_rtol = 0.001d0
70
71
72     ! atmosphere
73     atm_option = 'T_tau'
74     atm_T_tau_relation = 'Eddington'
75     atm_T_tau_opacity = 'fixed'
76
77
78
79     ! options for energy conservation (see MESA V, Section 3)
80     max_abs_rel_run_E_err = -1
81
82     mixing_length_alpha = 2.0
83     use_Ledoux_criterion = .false.
84
85
86
87
88     overshoot_scheme(1) = 'step'
89     overshoot_zone_type(1) = 'burn_H'
90     overshoot_zone_loc(1) = 'core'
91     overshoot_bdy_loc(1) = 'top'
92     overshoot_f(1) = 0.35
93     overshoot_f0(1) = 0.05
94
95
96
97     ! solver
98     ! options for energy conservation (see MESA V, Section 3)
99     !energy_eqn_option = 'eps_grav'
100    energy_eqn_option = 'dedt'
101    use_gold_tolerances = .true.
102
103
104    ! output interval
105    terminal_interval = 1
106    history_interval = 1
107    profile_interval = 1
108    max_model_number = -1
109    max_num_profile_models = 10
110    photo_digits = 5
111    photo_interval = 50
112
113
114
115

```

116 / ! end of controls namelist

Listing B.2: sample donor star inlist for methods 2 and 3

```
1 &binary_job
2
3   inlist_names(1) = 'inlist1 '
4   inlist_names(2) = 'inlist2 '
5
6   change_ignore_rlof_flag = .true.
7   change_initial_ignore_rlof_flag = .true.
8   new_ignore_rlof_flag = .true.
9
10  evolve_both_stars = .false.
11
12 / ! end of binary_job namelist
13
14 &binary_controls
15   terminal_interval = 100
16
17   m1 = 1.0d0 ! donor mass in Msun
18   m2 = 2.d0 ! companion mass in Msun
19   initial_period_in_days = -3.9d0
20
21   initial_separation_in_Rsuns = 6.23
22   initial_eccentricity = 0.0d0
23   do_tidal_circ = .true.
24   !!!!!!! if RLOF, it'll just stop
25   terminate_if_initial_overflow = .true.
26
27   mdot_scheme = 'roche_lobe'
28
29   limit_retention_by_mdot_edd = .true.
30
31   max_tries_to_achieve = 50
32
33   do_jdot_gr = .false.
34   do_jdot_ml = .true.
35   do_jdot_ls = .false.
36   do_jdot_missing_wind = .false.
37   do_jdot_mb = .false.
38
39
40   do_tidal_sync = .false.
41
42   do_initial_orbit_sync_1 = .false.
43
44
45 / ! end of binary_controls namelist
```

Listing B.3: sample binary controls inlist for method 2

```
1 &binary_job
2
```

```

3  inlist_names(1) = 'inlist1 '
4  inlist_names(2) = 'inlist2 '
5  change_ignore_rlof_flag = .true.
6  change_initial_ignore_rlof_flag = .true.
7  new_ignore_rlof_flag = .true.
8  evolve_both_stars = .false.
9
10 / ! end of binary_job namelist
11
12 &binary_controls
13   terminal_interval = 100
14
15   m1 = 7.0d0 ! donor mass in Msun
16   m2 = 3.5d0 ! companion mass in Msun
17   initial_period_in_days = -3.9d0
18
19   initial_separation_in_Rsuns = 45.45
20   initial_eccentricity = 0.0d0
21   do_tidal_circ = .true.
22   !!!!!!! if RLOF, it'll just stop
23   terminate_if_initial_overflow = .true.
24
25   mdot_scheme = 'roche_lobe'
26
27   limit_retention_by_mdot_edd = .true.
28
29   max_tries_to_achieve = 50
30
31   do_jdot_gr = .false.
32   do_jdot_ml = .true.
33   do_jdot_ls = .false.
34   do_jdot_missing_wind = .false.
35   do_jdot_mb = .false.
36
37   do_tidal_sync = .true. !!! for case 2 false
38
39   sync_type_1 = 'Instantaneous'
40
41   sync_mode_1 = 'Uniform'
42
43   do_initial_orbit_sync_1 = .true. !!! for case 2 false
44
45
46 / ! end of binary_controls namelist

```

Listing B.4: sample binary controls inlist for method 3

```

1 &star_job
2 ! see star/defaults/star_job.defaults
3
4 ! begin with a pre-main sequence model
5   create_pre_main_sequence_model = .false.
6 !   set_uniform_initial_composition=.true.
7 !   initial_zfracs = 3

```

```

8
9
10 ! save a model at the end of the run
11 save_model_when_terminate = .true.
12 save_model_filename = 'v1309_last.mod'
13
14 write_profile_when_terminate=.true.
15 filename_for_profile_when_terminate='profile_v1309_last.data'
16
17 ! control the output
18 history_columns_file = 'history_columns.list '
19 profile_columns_file = 'profile_columns.list '
20
21 ! display on-screen plots
22 pgstar_flag = .true.
23
24
25 change_initial_net = .true. ! switch nuclear reaction network
26 new_net_name = 'pp_and_cno_extras.net '
27 auto_extend_net = .true.
28 h_he_net = 'pp_and_cno_extras.net '
29 co_net = 'co_burn.net '
30 adv_net = 'approx21.net '
31
32
33 / ! end of star_job namelist
34
35
36 &eos
37 ! eos options
38 ! see eos/defaults/eos.defaults
39
40 / ! end of eos namelist
41
42
43 &kap
44 ! kap options
45 ! see kap/defaults/kap.defaults
46 use_Type2_opacities = .true.
47 Zbase = 2d-2
48 kap_file_prefix = 'OP_gs98'
49 kap_lowT_prefix = 'lowT_fa05_gs98' ! for lower temperatures.
50
51
52 / ! end of kap namelist
53
54
55 &controls
56 ! see star/defaults/controls.defaults
57
58 ! starting specifications
59 initial_mass = 1.52 ! in Msun units
60 initial_z = 0.02
61

```

```

62 ! when to stop
63 !max_age=2.4488+09
64 max_years_for_timestep = 1.e7
65
66
67 ! wind
68 hot_wind_scheme = 'Vink'
69 cool_wind_RGB_scheme = 'Reimers'
70 cool_wind_AGB_scheme = 'Blocker'
71 Vink_scaling_factor = 0.1d0
72 Reimers_scaling_factor = 0.1
73 Blocker_scaling_factor = 0.5
74 RGB_to_AGB_wind_switch = 1d-4
75 cool_wind_full_on_T = 0.8d4
76 hot_wind_full_on_T = 1.2d4
77
78 ! atmosphere
79 atm_option = 'T_tau'
80 atm_T_tau_relation = 'Eddington'
81 ! attention: the fitted envelope were obtained with Eddington option
82 ! above
83 ! which_atm_option = 'photosphere_tables'
84
85
86 ! rotation
87
88 ! element diffusion
89
90 ! mlt
91 ! convection set up
92 ! decrease of mixing length makes V1309 Sco progenitor cooler at the
93 ! same radius
94 ! value 1.88 reproduces as in the paper
95 mixing_length_alpha = 1.88
96 use_Ledoux_criterion = .true.
97 alpha_semiconvection = 0.001
98
99 overshoot_scheme(1) = 'step'
100 overshoot_zone_type(1) = 'any'
101 overshoot_zone_loc(1) = 'core'
102 overshoot_bdy_loc(1) = 'top'
103 overshoot_f(1) = 0.35
104 overshoot_f0(1) = 0.05
105
106 use_other_cgrav = .true.
107 ! stop when photosphere_r is greater than this limit, in R_sun units
108 photosphere_r_upper_limit = 3.70
109
110 ! tolerance of stop
111
112 when_to_stop_atol = 0d0
113 when_to_stop_rtol = 0.001d0

```

```

114
115
116 !!!!! inputs used in subroutines
117 !!mass ratio q= M1/M2
118   x_ctrl(1) = 10.d0
119 !! orbital separation of the binary in solar radii
120   x_ctrl(2) = 6.4d0
121
122
123   ! mixing
124
125   ! timesteps
126   limit_for_rel_error_in_energy_conservation = 1d-5
127   hard_limit_for_rel_error_in_energy_conservation = 1d-3
128   varcontrol_target = 1d-4
129   delta_lgTeff_limit = 0.0003d0
130   delta_lgTeff_hard_limit = -1
131   delta_lgL_limit_L_min = -100
132   delta_lgL_limit = 0.001d0
133   delta_lgL_hard_limit = -1
134
135   ! mesh
136
137   ! solver
138     ! options for energy conservation (see MESA V, Section 3)
139     energy_eqn_option = 'eps_grav'
140     use_gold_tolerances = .true.
141     max_abs_rel_run_E_err = 1.e10
142
143   ! output interval
144     terminal_interval = 1
145     history_interval = 1
146     profile_interval = 1
147     max_model_number = 5000
148     max_num_profile_models = 50
149 / ! end of controls namelist

```

Listing B.5: sample inlist for method 1 for the case of V1309 Scorpii